IRAQI JOURNAL OF APPLIED PHYSICS

The *Iraqi Journal of Applied Physics (IJAP)* is a peer reviewed journal of high quality devoted to the publication of original research papers from applied physics and their broad range of applications. IJAP publishes quality original research papers, comprehensive review articles, survey articles, book reviews, dissertation abstracts in physics and its applications in the broadest sense. It is intended that the journal may act as an interdisciplinary forum for Physics and its applications. Innovative applications and material that brings together diverse areas of Physics are particularly welcome. Review articles in selected areas are published from time to time. It aims to disseminate knowledge; provide a learned reference in the field; and establish channels of communication between academic and research experts, policy makers and executives in industry, commerce and investment institutions. IJAP is a quarterly specialized periodical dedicated to publishing original papers, letters and reviews in: Applied & Nonlinear Optics, Applied Mechanics & Thermodynamics, Digital & Optical Communications, Electronic Materials & Devices, Laser Physics & Applications, Plasma Physics & Applications, Quantum Physics & Spectroscopy, Semiconductors & Optoelectronics, and Solid State Physics & Applications

EDITORIAL BOARD

Dayah N. RAOUF
Editor-in-Chief
School of Applied Sciences
University of Technology, IRAQ
dayah@ijap.org

Walid K. HAMOUDI
Member
School of Applied Sciences,
University of Technology, IRAQ
walid@ijap.org

Raid A. ISMAIL
Member
Ministry of Science and
Technology, Baghdad, IRAQ
raid@ijap.org

Raad A. KHAMIS
Member
School of Applied Sciences
University of Technology, IRAQ
raad@ijap.org

Oday A. HAMADI
Managing Editor
P. O. Box 55159,
Baghdad 12001, IRAQ
oday@ijap.org

Rania A. MARKUB
Middle East Coordinator
P. O. Box 55259,
Baghdad 12001, IRAQ
rania@ijap.org

Haitham M. MIKHLIF
Reviews Editor
Department of Physics,
Al-Mustansiriya University, IRAQ
haitham@ijap.org

Intesar F. RAMLEY
Industrial Relation Coordinator
INToo Software, Vancouver,
V4B 4W4, BC, Canada
intesar@ramley.com

Editorial Office
P. O. Box 55259,
Baghdad 12001,
IRAQ
Website: **www.ijap.org**
Email: **editor@ijap.org**
Tel.: **00964 7901274190**

ADVISORY BOARD

Xueming LIU
Professor
Department of Electronic Engineering,
Tsinghua University, Beijing, CHINA

Mansoor SHEIK-BAHAE
Associate Professor
Department of Physics and Astronomy,
University of New Mexico, U.S.A

Shivaji H. PAWAR
Professor
D. Y. Patil University, Kasaba Bawada,
Kolhapur-416 006, INDIA

Franko KUEPPERS
Professor
College of Optical Sciences,
University of Arizona, Tucson, U.S.A

Yushihiro TAGUCHI
Professor
Department of Physics, Chuo University,
Bunkyo-ku, Tokyo, JAPAN

El-Sayed M. FARAG
Professor
Department of Sciences, College of
Engineering, Al-Minofiya University, EGYPT

Mutaz S. ABDUL-WAHAB
Assistant Professor
Electric and Electronic Engineering,
University of Technology, Baghdad, IRAQ

Mazin M. ELIAS
Professor
Laser Institute for Postgraduates
University of Baghdad, Baghdad, IRAQ

Kais A. AL-NAIMEE
Assistant Professor
National Institute of Applied Optics, Phys.
Dep., University of Florence, Florence, Italy

Muhammad A. HUSSAIN
Assistant Professor
Department of Laser and Optoelectronics
Engineering, Al-Nahrain University, IRAQ

Chang Hee NAM
Professor
Korean Advanced Institute of Science
and Technology, Taejon, KOREA

Ashok KUMAR
Professor
Harcourt Butler Technological Institute,
Kanpur-208 002, INDIA

Marc BURGELMAN
Professor
Electronics and Information Systems,
University of Gent, Gent, BELGIUM

Heidi ABRAHAMSE
Professor
Faculty of Health Sciences, University
of Johannesburg, SOUTH AFRICA

Andrei KASIMOV
Professor
Institute of Material Science, National
Academy of Science, UKRAINE

Yanko SAROV
Assistant Professor
Micro- and Nanoelectronic Systems,
Technical University Ilmenau, GERMANY

Mohammed A. HABEEB
Professor
Department of Physics, Faculty of
Science, Al-Nahrain University, IRAQ

Abdullah M. SUHAIL
Assistant Professor
Department of Physics, College of
Science, University of Baghdad, IRAQ

Khaled A. AHMED
Assistant Professor
Department of Physics, College of Science,
Al-Mustansiriya University, IRAQ

Manal J. AL-KINDY
Assistant Professor
Department of Electronic Engineering,
Al-Nahrain University, IRAQ

SPONSORED AND PUBLISHED BY
THE IRAQI SOCIETY FOR ALTERNATIVE AND RENEWABLE ENERGY SOURCES & TECHNIQUES (I.S.A.R.E.S.T.)

IRAQI JOURNAL OF APPLIED PHYSICS
" INSTRUCTIONS TO AUTHORS "

CONTRIBUTIONS
Contributions to be published in this journal should be original research works, i.e., those not already published or submitted for publication elsewhere, individual papers or letters to editor.

SUBMISSION OF MANUSCRIPTS
Manuscripts should be submitted to the editor at the mailing address:

Iraqi Journal of Applied Physics, Editorial Board
P. O. Box 55259, Baghdad 12001, IRAQ, submission@ijap.org **,** editor@ijap.org

MANUSCRIPTS
Two hard copies with soft copy on a compact disc (CD) should be submitted to Editor in the following configuration:

- Double-spaced one-side A4 size with 2.5 cm margins of all sides
- Times New Roman font (16pt bold for title, 14pt bold for names, 12pt bold for headings, 12pt regular for text)
- Letters should not exceed 10 pages, papers should not exceed 20 pages and reviews are up to author.
- Manuscripts presented in English only are accepted.
- English abstract not exceed 150 words
- 4 keywords (at least) should be maintained on (PACS preferred)
- Author(s) should express all quantities in SI units
- Equations should be written in equation form (*italic* and symbolic)
- Figures and Tables should be separated from text
- Figures and diagrams can be submitted in colors for assessment and they will be returned to authors after provide printable copies
- Charts should be indicated by the software used for
- Only original or high-resolution scanner photos are accepted
- For electronic submission, articles should be formatted with MS-Word software.

AUTHOR NAMES AND AFFILIATIONS
It is IJAP policy that all those who have participated significantly in the technical aspects of a paper be recognized as co-authors or cited in the acknowledgments. In the case of a paper with more than one author, correspondence concerning the paper will be sent to the first author unless staff is advised otherwise.

Author name should consist of first name, middle initial, last name. The author affiliation should consist of the following, as applicable, in the order noted:

- Company or college (with department name or company division)
- Postal address
- City, state, zip code
- Country name
- Telephone, and e-mail

REFERENCES
The references should be brought at the end of the article, and numbered in the order of their appearance in the paper. The reference list should be cited in accordance with the following examples:

[1] X. Ning and M.R. Lovell, "On the Sliding Friction Characteristics of Unidirectional Continuous FRP Composites", *ASME J. Tribol.*, 124(1) (2002) 5-13.

[2] M. Barnes, "Stresses in Solenoids", *J. Appl. Phys.*, 48(5) (2001) 2000–2008.

[3] J. Jones, "Contact Mechanics", Cambridge University Press (Cambridge, UK) (2000), Ch.6, p.56.

[4] Y. Lee, S.A. Korpela and R. Horne, "Structure of Multi-Cellular Natural Convection in a Tall Vertical Annulus", Proc. 7th International Heat Transfer Conference, U. Grigul et al., eds., Hemisphere (Washington DC), 2 (1982) 221–226.

[5] M. Hashish, "Waterjet Technology Development", High Pressure Technology, PVP-Vol. 406 (2000), 135-140.

[6] D.W. Watson, "Thermodynamic Analysis", ASME Paper No. 97-GT-288 (1997).

[7] C.Y. Tung, "Evaporative Heat Transfer in the Contact Line of a Mixture", Ph.D. thesis, Rensselaer Polytechnic Institute, Troy, NY (1982).

PROOFS
Authors will receive proofs of papers and are requested to return one corrected hard copy with a WORD copy on a compact disc (CD). New materials inserted in the original text without Editor permission may cause rejection of paper.

COPYRIGHT FORM
Author(s) will be asked to transfer copyrights of the article to the Journal soon after acceptance of it. This will ensure the widest possible dissemination of information.

OFFPRINTS
Authors will receive offprints free of charge and any additional offprints can be ordered.

SUBSCRIPTION AND ORDERS
Annual fees (4 issues per year) of subscription are:

- 50 US$ for individuals inside Iraq.
- 100 US$ for establishments inside Iraq.
- 100 US$ for individuals abroad.
- 200 US$ for establishments abroad.

Fees are reduced by 25% for I.S.A.R.E.S.T. members. Orders of issues can be submitted by contacting the editor-in-chief or editorial office at **subscription@ijap.org** to maintain the address of issue delivery and payment way.

Fawwaz J. Jibrael
Atheer A. Sabri
Shahad D. Sateaa

Department of Electrical and
Electronic Engineering,
University of Technology,
P. O. Box 35010,
Baghdad, Iraq

Dipole Antenna with Fractal Koch Curve Geometry for Multiple Frequency Applications

This paper presents the analysis, simulation, and design of a small size, low profile, multi-band third iteration quadratic Koch fractal dipole antenna. The proposed antenna design, analysis and characterization have been performed using the method of moments (MoM) technique. The new designed antenna has operating frequencies of 960 MHz, 1514 MHz, 2914 MHz, 3274 MHz, and 3480 MHz with acceptable bandwidth, which has useful applications in wireless communication systems, and at these frequencies the proposed antenna has reflection coefficient <-10dB (vswr<2). The radiation characteristics, vswr, gain, radiation efficiency, and reflection coefficient of the proposed antenna are described and simulated using 4nec2 software package.

Keywords: Fractal geometry, Dipole antenna, Multiband antenna, Quadratic Koch curve
Received: 14 March 2011, **Revised**: 23 May 2011, **Accepted**: 01 June 2011

1. Introduction

Modern telecommunication systems require antennas with wider bandwidths and smaller dimensions than conventionally possible. This has initiated antenna research in various directions, one of which is by using fractal shaped antenna elements. In recent years several fractal geometries have been introduced for antenna applications with varying degrees of success in improving antenna characteristics. Some of these geometries have been particularly useful in reducing the size of the antenna, while other designs aim at incorporating multi-band characteristics. These are low profile antennas with moderate gain and can be made operative at multiple frequency bands and hence are multi-functional [1].

Fractal geometry was first discovered by Benoit Mandelbrot as a way to mathematically define structures whose dimension cannot be limited to whole numbers. Benoit Mandelbrot [2], the pioneer of classifying this geometry, first coined the term 'fractal' in 1975 from the Latin word fractus, which means broken. The field is quite extensive with many applications from statistical analyses, natural modeling, compression and, of course, computer graphics [3]. Soon after scientists discovered the practical aspect of fractal geometry, research began in the field of electrodynamics [4-8].To date most efforts have been concentrated in understanding the physical process and mathematical background of interaction between electromagnetic waves and fractal structures.

These geometries have been used to characterize structures in nature that were difficult to define with Euclidean geometries. Examples include the length of a coastline, the density of clouds, and the branching of trees. Just as nature is not confined to Euclidean geometries, antennas and antennas array designs should not be confined, as well. In addition to having non-integer dimension, fractals usually exhibit some form of self-similarity which means that they are composed only of multiple copies of themselves at several scales. These properties can be used to develop new configurations for antennas and antenna arrays [9]. It might be possible to discover structures that give us better performance than any Euclidean geometry could provide. Fractals represent a class of geometry with very unique properties that can be enticing for antenna designers [10].

Fractals are space filling contours, meaning electrically large features can be efficiently packed into small areas [3]. Since the electrical lengths play such an important role in antenna design, this efficient packing can be used as a viable miniaturization technique. Fractals are structures of infinite complexity with a self-similar nature. What this means, is that as the structure is zoomed in upon, the structure repeats itself. This property could be used to design antennas that can operate at several frequencies.

Fractal antenna theory uses a modern (fractal) geometry that is a natural extension of Euclidian geometry. A fractal can fill the space occupied by the antenna in a more effective manner than the traditional Euclidean antenna. This can lead to more effective coupling of energy from feeding transmission lines to free space in less volume. Therefore, fractals can be used in two ways to enhance antenna designs. The first method is in the design of miniaturized antenna elements. These can lead to antenna elements which are more discrete for the end user. The second method is to use the self-similarity in the geometry to blueprint antennas which are multiband or resonant over several frequency bands [11-12]. This would allow the operator to incorporate several aspects of their system into one antenna. Such antennas could be used to improve the functionality of modern wireless communication receivers such as cellular handsets. Because fractal antennas are more compact, they would more easily in the receiver package [10].

Other applications included fractal miniaturization of passive networks and components, fractal filters and Resonators [13]. A fractal element antenna, or FEA, is one that has been shaped in a fractal fashion, either through bending or shaping a volume, or introducing holes. They are based on fractal shapes such as the Sierpinski triangle. Mandelbrot tree, Koch curve, and Koch island. The advantage of FEAs, when compared to conventional antenna designs, center around size and bandwidth.

This paper presents the design and simulation a wire dipole antenna based on the third iteration quadratic Koch curve geometry.

2. Generation of Quadratic Koch Curve

Figure (1) contains the first three iterations in the construction of the quadratic Koch curve. This curve is generated by repeatedly replacing each line segment, composed of four quarters, with the generator consisting of eight pieces, each one quarter long (see Fig. 1) [14]. Each smaller segment of the curve is an exact replica of the whole curve.

There are eight such segments making up the curve, each one represents a one-quarter reduction of the original curve. Different from Euclidean geometries, fractal geometries are characterized by their non-integer dimensions. Fractal dimension contains used information about the self similarity and the space-filling properties of any fractal structures [15]. The fractal similarity dimension (*FD)* is defined as [14]:

$$FD = \frac{\log(N)}{\log(\frac{1}{\varepsilon})} = \frac{\log(8)}{\log(4)} = 1.5$$

where N is the total number of distinct copies, and $(1/\varepsilon)$ is the reduction factor value which means how will be the length of the new side with respect to the original side length.

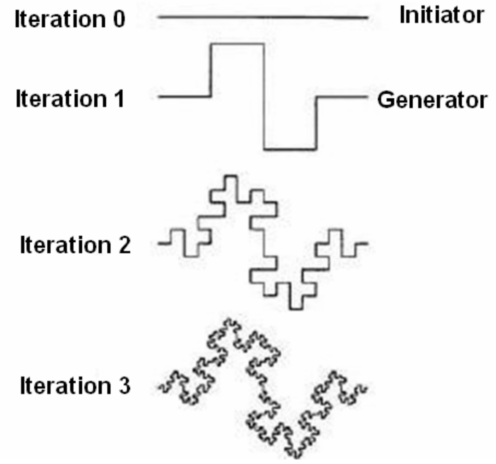

Fig. (1) First three iterations of the construction of the quadratic Koch curve

3. Proposed Antenna Design and Simulation Results

The numerical simulations of the antenna system are carried out via the method of moments. Numerical modeling commercial software 4nec2 is used in all simulations. The nec is a computer code based on the method of moment for analyzing the electromagnetic response of an arbitrary structures consisting of wires or surfaces, such as Hilbert and Koch curves. The modeling process is simply done by dividing all straight wires into short segments where the current in one segment is considered constant along the length of the short segment. It is important to make each wire segment as short as possible without violation of maximum segment length to radius ratio computational restrictions. In nec, to modeling a wire structures, the segments should follows the paths of conductor as closely as possible [16].

The proposed antenna is shown in Fig. (2). The proposed antenna is placed in YZ-plane with design frequency equal to 750 MHz. The feed source point of this antenna is placed at the origin (0,0,0), and this source is set to 1 volt. For the design frequency of 750 MHz, the design wavelength, λ is 0.4 m (40 cm) then the length of the corresponding λ/2 dipole antenna length will be of 20 cm.

The vswr and reflection coefficient of the third iteration quadratic Koch dipole antenna is shown in Figures (3) and (4) respectively. It is found that the antenna has multiband behavior at the resonance frequencies 960 MHz, 1514 MHz, 2914 MHz, 3274 MHz, and 3480 MHz with acceptable bandwidth and reflection coefficient <-10 dB (vswr<2).

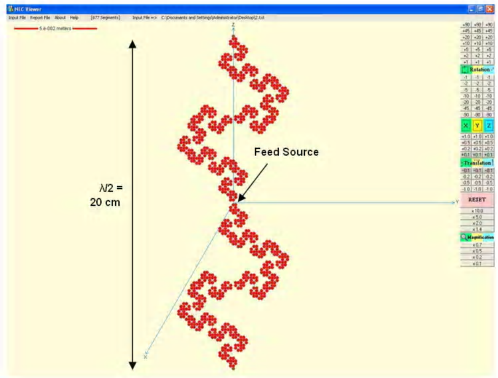

Fig. (2) Proposed fractal dipole antenna

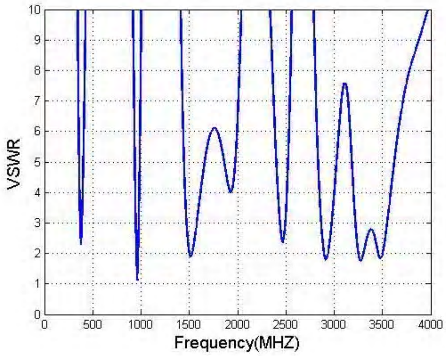

Fig. (3) Simulated 50Ω, vswr vs. frequency

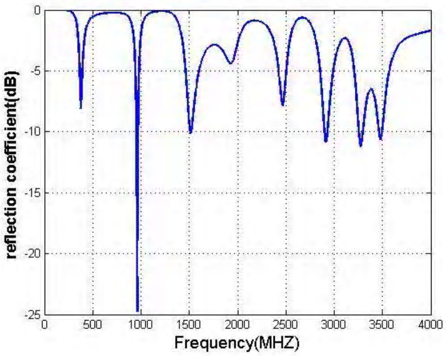

Fig. (4) Reflection coefficients at the antenna terminals

The three dimensional gain radiation patterns at the resonant frequencies for the proposed antenna have been illustrated in Fig. (5).

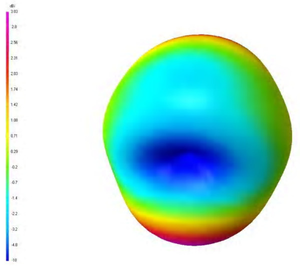

(a) f = 960 MHz

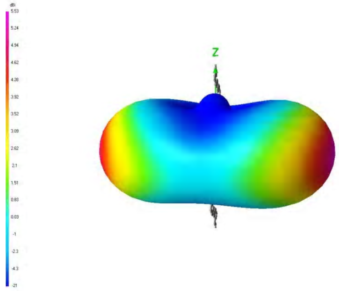

(b) f = 1514 MHz

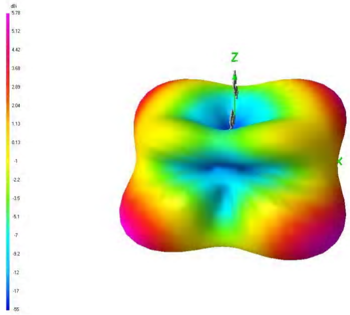

(c) f = 2914 MHz

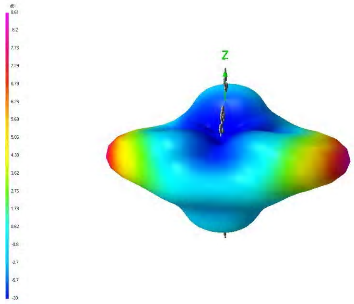

(d) f = 3274 MHz

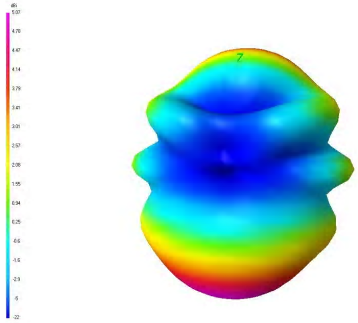

(e) f = 3480 MHz

Fig. (5) 3D gain radiation pattern at *f*= (a) 960 (b) 1514 (c) 2914 (d) 3274 (e) 3480 MHz

Table (1) shows these resonant frequencies, vswr, gain, radiation efficiency, and reflection coefficients for each frequency.

The electric field radiation patterns at these resonant frequencies in the planes YZ-plane, XZ-plane, and XY-plane are depicted in Figure 6, when the antenna is placed in the YZ-plane.

4. Conclusion

In this work, the quadratic Koch curve dipole antenna, based on the 3rd iteration, is investigated and its performance is evaluated. The simulation results show that this antenna can be efficiently operated as a multiband antenna and is compact in size. The proposed antenna has five resonance bands at frequencies of 960 MHz, 1514 MHz, 2914 MHz, 3274 MHz, and 3480 MHz, and at these frequencies the antenna has vswr<2 (reflection coefficient <-10dB), high gain, and high radiation efficiency. According to these frequencies, this antenna can operate as a multiband antenna in the UHF/SHF applications.

References

[1] Jaspreet K., "Sierpinski Gasket: Multiband Fractal Antenna for 4G Systems", Master of Engineering Thesis, Thapar University, India, June (2010).

[2] Mandelbrot, B.B, "The Fractal Geometry of Nature", W.H. Freeman and Company, New York. (1983).

[3] Gianvittorio J.P., "Fractals, MEMS and FSS Electromagnetic Devices: Miniaturization and Multiple Resonances", Ph.D. Dissertation, University of California, Los Angeles, August (2003).

[4] D.L. Jaggard, "On Fractal Electrodynamics", in H.N. Kritikos and D.L. Jaggard (eds.), Recent Advances in Electromagnetic Theory, New York, Springer-Verlag, (1990), pp. 183-224.

[5] D.L. Jaggard, "Fractal Electrodynamics and Modelling", in H.L. Bertoni and L.B. Felson (eds.), Directions in Electromagnetic Wave Modelling, New York, Plenum Publishing Co. (1991), pp. 435-446.

[6] D.L. Jaggard, "Fractal Electrodynamics: Wave Interactions with Discretely Self-Similar Structures", in C. Baum and H. Kritikos (eds.), Electromagnetic Symmetry, Washington DC, Taylor and Francis Publishers, (1995), pp. 231-281.

[7] D.H. Werner, "An Overview of Fractal Electrodynamics Research", in Proceedings of the 11th Annual Review of Progress in Applied Computational Electromagnetics (ACES), Volume II, Naval Postgraduate School, Monterey, CA, March, (1995), pp. 964-969.

[8] D.L. Jaggard, "Fractal Electrodynamics: From Super Antennas to Superlattices", in J.L. Vehel, E. Lutton, and C. Tricot (eds.), Fractals in Engineering, New York, Springer-Verlag, (1997), pp. 204-221.

[9] Anguera, J. et al., *Microwave Optic. Technol. Lett.*, 37(2) (2003) 100-103.

[10] D. Kalra, "Antenna Miniaturization Using Fractals", Master of Engineering Thesis, Thapar Institute of Engineering & Technology (Deemed University), India, (2007).

[11] Song, C.T., Hall, P.S. and Ghafouri-Shiraz, H., *IEEE AP-S Trans.*, 51(4) (2003) 722-729.

[12] Anguera, J. et al., *IEEE Trans Antennas Propag.*, 54(11) (2006) 3367-3373.

[13] Fractus, The Technology of Nature, URL: www.Fractus.com

[14] K. Falconer, **"Fractal Geometry; Mathematical Foundations and Applications,"** 2nd ed., John-Wiley & Sons Ltd. (2003).

[15] P.S. Addison, **"Fractals and Chaos"**, Institute of Physics Publishing, London (1997).

[16] G.J. Burke and A.J. Poggio "Numerical Electromagnetic Code (NEC)-Program description", Lawrence Livermore Laboratory, January (1981).

Table (1) Simulation results of the Proposed Antenna

Frequency (MHz)	vswr	Reflection Coefficient (dB)	Peak Gain (dBi)	Bandwidth (MHz)	Radiation Efficiency (%)
960	1.12319	-24.728	3.03	20	94.02
1514	1.90539	-10.127	5.53	14	93.3
2914	1.79949	-10.885	5.78	35	95.98
3274	1.7583	-11.216	8.61	47	95.69
3480	1.83305	-10.632	5.07	36	92.36

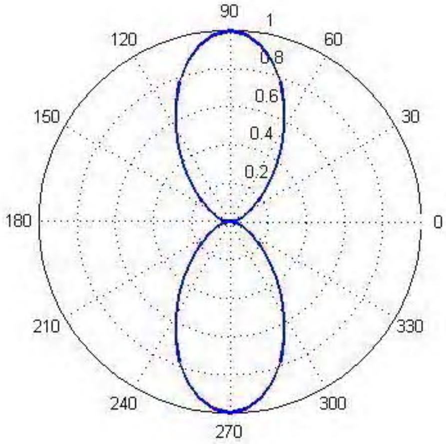

XZ-Plane

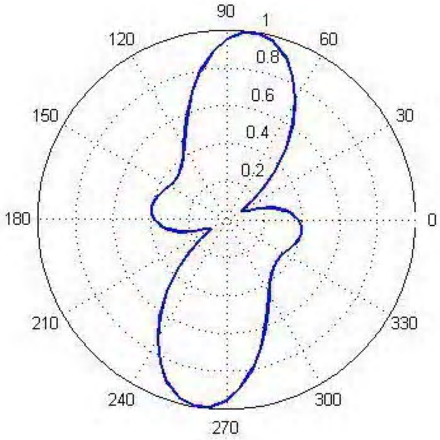

YZ-Plane

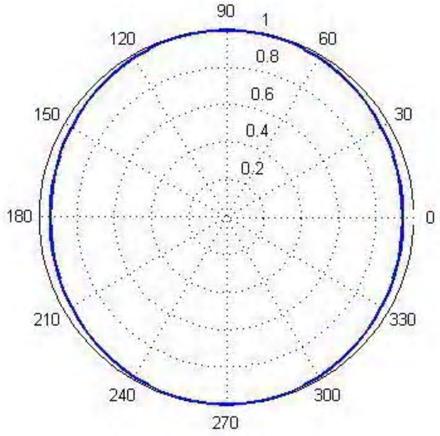

XY-Plane
(b) f = 1514 MHz

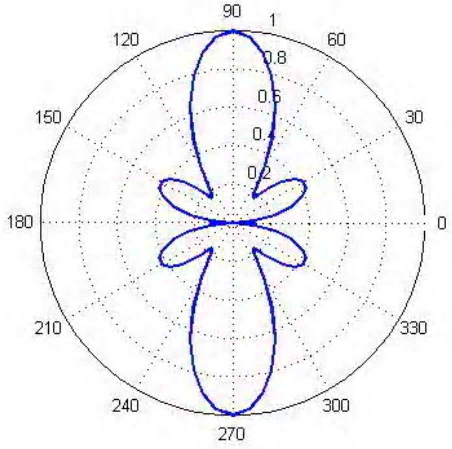

XZ-Plane

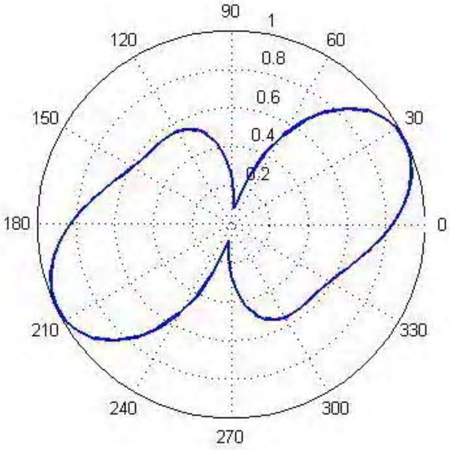

YZ-Plane

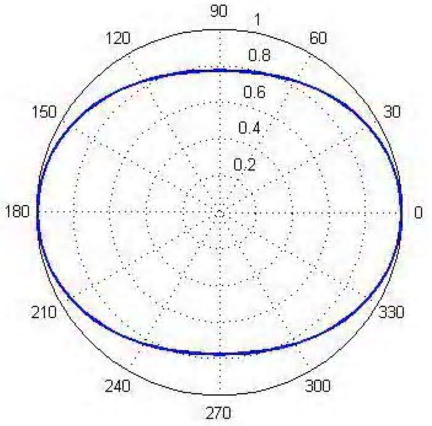

XY-Plane
(a) f = 960 MHz

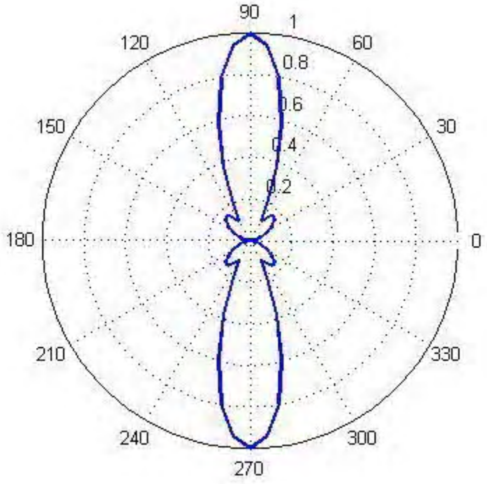

XZ-Plane

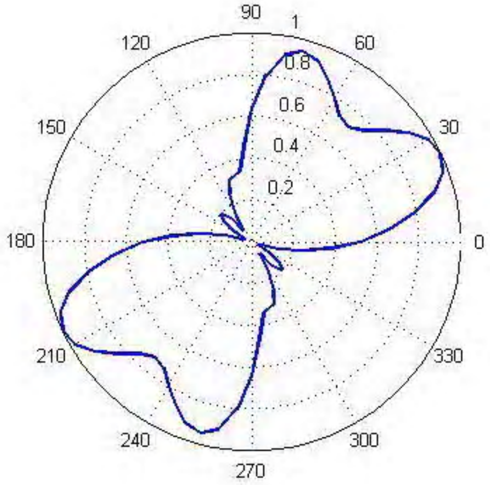

YZ-Plane

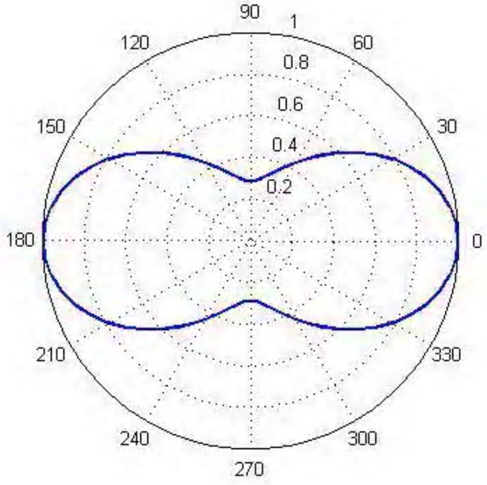

XY-Plane
(d) f = 3274 MHz

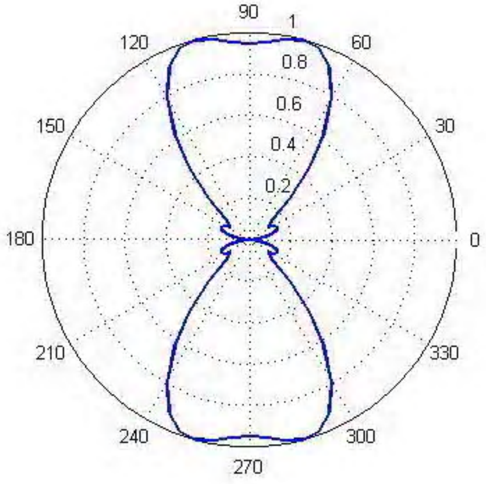

XZ-Plane

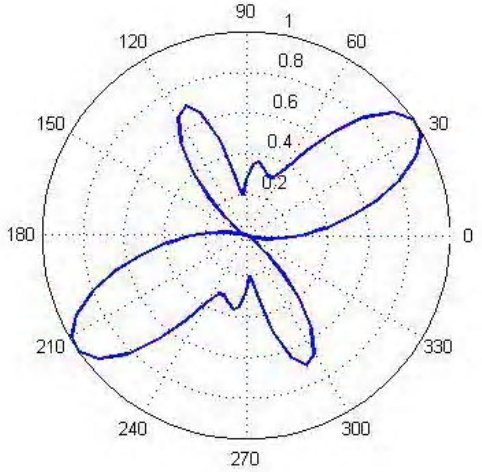

YZ-Plane

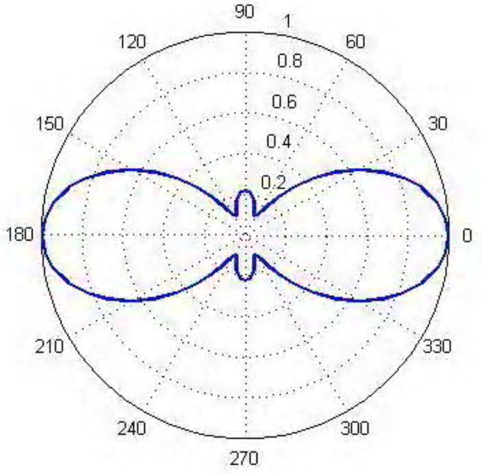

XY-Plane
(c) f = 2914 MHz

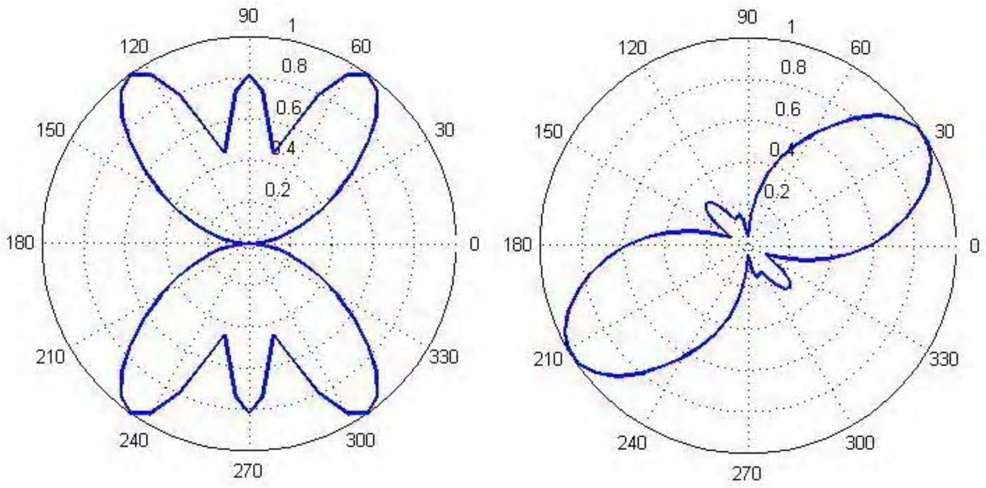

XZ-Plane **YZ-Plane**

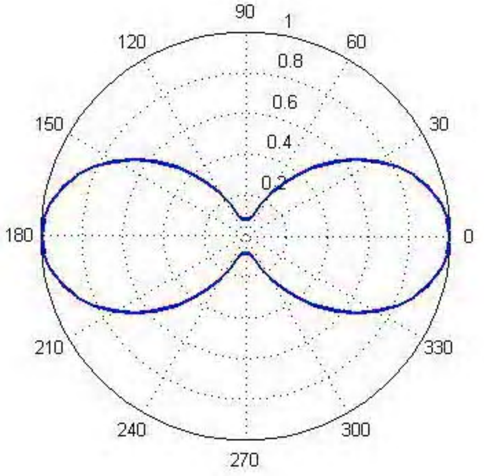

XY-Plane
(e) f = 3480 MHz

Fig. (6) Radiation Patterns of the proposed antenna at Resonant Frequencies of *f*= (a) 960 MHz (b) 1514 MHz (c) 2914 MHz (d) 3274 MHz (e) 3480 MHz

---

This article was reviewed at South Dakota School of Mines and Technology, 501 E St Joseph Street, Rapid City, SD, 57701, U.S.A, and Department of Electronics and Telecommunications, Universitat Ramon LLull, Barcelona, SPAIN

ETOP2012

29-31 March 2012 - Tunis - Tunisia

Sponsors:

EDUCATION AND TRAINING IN OPTICS AND PHOTONICS " ETOP2012 "

29-31 March 2012 - Tunis - Tunisia

ABOUT ETOP

ETOP (Education and Training in Optics & Photonics) is a biennal conference that brings together educators from around the world to share information about the practice of teaching optics at all levels. The teaching of optics and photonics, critical fields at the core of today's world-wide technological infrastructure, must continually be upgraded and renewed in order to meet the growing demands of research, science & industry. It is the goal of this international conference to bring together leading optics and photonics educators from all levels and orientations to discuss, demonstrate and learn about new developments and approaches to teaching in these fields.

Typical session topics include :

- Education and technological education in optics and photonics (geometrical optics, electromagnetic optics, quantum optics, biomedical optics, integrated optics, diffractive optics, software for teaching, Computer assisted learning)
- Technician Training and laboratory materials for demonstrations,
- Training and continuing education in collaboration with industry (Entrepreneurship for optics and photonics, student projects in optics and photonics, Olympiads, …)
- New pedagogical methods, tools and models for education in optics & photonics
- Curriculum development laboratories for optics and photonics education
- Education and training for inter and multidisciplinary applications. Optics curricula in biomedical optics, micro and nanotechnology and other emerging fields.

Proceedings of ETOP

All past proceedings of ETOP conferences are available as PDFs online. For **free PDFs** of the papers presented at previous ETOP conferences click on : spie.org/etop

Apply to Host a Future ETOP Conference

The ETOP conference takes place every two years and it is the aim of the sponsors to make this critical information equally available to both developed and developing countries. In order to ensure world-wide participation, the sponsors (ICO, LEOS, SPIE and OSA) welcome and encourage their chapters, affiliated bureaus, sections and other interested organizations to apply to host future ETOP conferences. To download an ETOP application form click on: Application to Host ETOP

ETOP 2012 will be followed from : Saturday 31 March to Tuesday 3 April 2012 by an EOS conference organized with Tunisian Society of Optics: «1st EOS Topical meeting on photonics for sustainable Development-Focus on the Mediterranean PSDM2012»

Adel K. Hamoudi[1]
Walid K. Hamoudi[2]
Saad A. Salih[3]

[1]*Department of Physics, College of Science, University of Baghdad, Baghdad, Iraq*
[2]*School of Applied Sciences, University of Technology, Baghdad, Iraq*
[3]*Department of Laser Engineering, College of Engineering, Al-Nahrain University, Baghdad, Iraq*

HAZ and Melt Limits of 3-D CO_2 Laser Welding

An analytical and numerical 3-D model for keyhole CO_2 laser welding of thick C/Mn steel sheets is constructed to study the heat affected zone (HAZ) and melt limits. Simulation results are compared with experimental investigations under variety of laser material processing conditions. The model combines a moving point source for the top part of the weld and a moving line source for the parallel sided region of the weld. The good match of theoretical and experimental results makes the model a good tool to predict the HAZ volume in which microstructure changes may occur. Such prediction is useful in the investigation of hardening and the cracks formation during laser welding.

Keywords: Laser welding, HAZ, Melt limit, 3D modeling, Keyhole welding
Received: 27 April 2010, **Revised**: 01 October 2010, **Accepted**: 01 June 2011

1. Introduction

Laser welding of metals has become critical in manufacturing processes and can provide a unique means of joining materials at high speeds with minimum thermal distortion and metallurgical damage [1,2]. The material interaction with laser light represents a delicate balance between heating and cooling within a spatially localized volume overlapping two or more solids such that a liquid pool is formed and remains stable until solidification. The intent in laser welding is to produce the liquid melt pool by absorption of incident radiation, allowing it to grow to the desired size, and then to propagate this melt pool through the solid interface between the components to be joined [3, 4]. Unsuccessful results are obtained if the melt pool is too large or too small or if significant vaporization occurs. Maintenance of the balance between heat input and heat output depends on the constant absorption of laser radiation and uniform dissipation of heat inside the work piece. The quality of the weld is affected by vaporization of alloying elements where excessive thermal gradients may lead to cracking on solidification and instabilities in the volume and geometry of the weld pool that can result in porosity and void formation [4]. Laser welding produces three distinct regions**:** the base metal, the fusion zone (weld pool) and the heat affected zone (HAZ) which represents a volume of the base metal that has been changed in some measurable way by welding [5-7]. In laser welding, one is often concerned about performing the process with minimum possible amount of heat. From this stand point, two mechanism of welding can be achieved: firstly, in the "conduction-limited welding mode ", the laser acts as a point source of energy moving across the surface of the work piece where the welds formed by this process are roughly semicircular in cross section, and secondly in the "keyhole welding mode", the laser acts as a line source of energy penetrating into the body of the material. This line source travels across the sheet producing welds that are narrow and deep [8, 9]. The keyhole surrounded by a molten region most of which flows round the keyhole and re-solidifies in the rear to form the weld. The keyhole is kept open by the excess vapor pressure as a whole over the sum of the hydrostatic pressure in the liquid metal and the surface tension force tending to close the keyhole [10]. The transition from conduction limited to keyhole welding is determined to a large extent by the energy density of the beam and the interaction time.

Laser beam butt welding was carried out for 1.6mm thick austenitic stainless steel at different beam power, welding speed and beam angle. A 3-D moving heat source and finite element code were used to calculate transient temperature profiles and weld pool dimensions, depth of penetration and weld width [11]. The formability of YAG and diode laser welded blanks of dual phase steel with banded martensite was investigated. It was found that the HAZ softened zone in dual phase steel weld completely dominated the fracture pattern [12]. Mild steel plates were welded by 1 kW CO_2 laser welding at different speeds and subjected to low ultrasound power to enhance the heat transfer by conduction and convection. It was found that heating, due to conduction, results in a relatively large weld bead and HAZ leading to a lower thermal gradient but when transferring heat to the HAZ at a higher rate more metal melted [13]. In a previous publication, a mathematical 3-D model for keyhole CO_2 laser welding of thick C/Mn steel sheets was constructed [14]. In the present work, numerical solutions of HAZ and melt limits are compared with results obtained from the experiments.

2. Theoretical background

The heat affected zone, HAZ is the area adjacent to the weld which has had its microstructure and properties altered by welding. The heat from the welding process and subsequent re-cooling causes this change in the area surrounding the weld. The extent and magnitude of property change depends primarily on the base material and the amount and concentration of heat input by the welding process. If the thermal diffusivity of the base material is high, the material cooling rate is high and the HAZ is relatively small. Alternatively, a low diffusivity leads to slower cooling and a larger HAZ. Laser welding gives a highly concentrated limited amount of heat, resulting in a small HAZ. In the same context, HAZ displays the effect of temperature cycling to a peak temperature, $T_{max,}$ which is less than the melting point but may be sufficient to initiate phase transformations. The cooling rate in the HAZ may approach 1000 °C/sec but varies with location, as does T_{max}. Under conduction-limited welding, the temperature at the center of the beam focus, r = 0, is [2, 15]:

$$T(0,t) - T_0 = \frac{AI_0\omega}{k(2\pi)^{\frac{1}{2}}} \tan^{-1}\left(\frac{8Kt}{\omega^2}\right)^{\frac{1}{2}} \qquad (1)$$

where I_0 is the incident laser intensity, T_0 is the ambient temperature, t is irradiation time, A is the absorptivity, k is the thermal conductivity, K is the thermal diffusivity, and ω is the Gaussian beam radius

If $T(0,t)=T_m$, the melting temperature, then the laser melting intensity, $I_m(0)$, required in time t can be obtained from equation (1). $I_m(0)$ is essentially independent of time when $t \gg \omega^2/8K$ or when the thermal diffusion length $\ell \approx (Kt)^{1/2} \gg \omega$. The radius of the beam focus on the surface, ω, will have profound effect on $I_m(0)$ when t is long, but has no effect at short irradiation times. When the work piece is moved at a speed U, relative to a stationary laser beam delivering an absorbed power, AP, to the surface, the threshold for conduction welding can be obtained from the following approximate solution to the heat equation [2,16,17]

$$T(r) - T_0 \approx \frac{AP}{2\pi Kr} \exp\left[-\left(\frac{U(x+r)}{1k}\right)\right] \qquad (2)$$

where the coordinate system is as shown in Fig. (1) and $r=(x^2+y^2+z^2)^{1/2}$

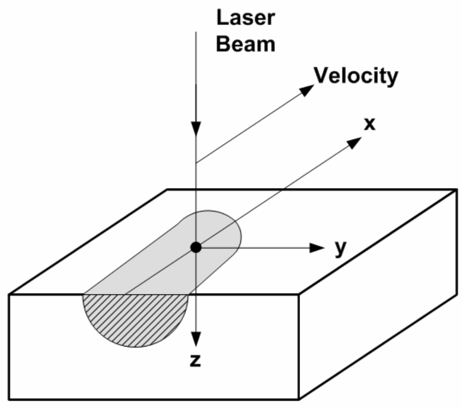

Fig. (1) Coordinate system for laser beam heating by a scanning source

The formation of a keyhole is possible when only high intensities of laser beams are used. Welds produced in this way often have aspect ratios (depth/width) of almost 10/1 or more. To obtain such high aspect ratio, the laser needs to act as a line source of energy throughout the depth of the material rather than point source acting, from the top surface only. This keyhole takes the form of a narrow deep hole surrounded by molten metal [17-19]. As the melt becomes rapidly heated by the laser, a severe thermal gradient is setup. The center of the melt approaches the boiling point while the edge remains at the melting point. [4,5]**.** This thermal gradient is associated with a surface tension gradient. The higher surface tension at the relatively cool edges of the melt acts to pull the liquid away from the center which causes the geometry to change, Fig. (2).

The shape of the melt improves the absorptivity in that area and this causes temperature to rise further. The increase in central temperature amplifies the depth of the central depression by a combination of surface tension effects and the initiation of surface boiling which increases the pressure on the center of the melt. The depression depth amplification continues until a keyhole is formed (Fig. 2c). The narrow deep hole is prevented from collapsing by the vapor pressure of the boiling liquid surrounding it. For a planar surface and an incident beam with a Gaussian intensity profile, the temperature at the center of the beam focus (r=0) is given by Eq. (1) except that $T(0,t)=T_v$ the vaporization temperature, thus:

$$T_v - T_0 = \frac{AI_0\omega}{k_v(2\pi)^{1/2}} \tan^{-1}\left[\frac{8K_v t}{\omega^2}\right]^{1/2} \qquad (3)$$

The linear vaporization rate (speed) in this case is:

$$V^* = \frac{\beta(T)}{\rho} \qquad (4)$$

where $\beta(T)$ is the mass evaporation rate**,** ρ is the metal density [2,9]

At the onset of vaporization, where laser intensity is highest, gas is ejected from the center of the weld pool in the case of a Gaussian or quasi–Gaussian laser intensity distribution [6,17]. The liquid is then subjected to a recoil pressure equal to the vapor pressure, P(T):

$$P(T) = \beta(T)\left[\frac{2\pi k_B T}{\overline{m}}\right]^{1/2} \qquad (5)$$

and will flow from the center of the weld pool out toward the periphery. Here k_B is Boltzman's constant, $\overline{m}$ is the average mass of an evaporating atoms, and T is the surface temperature.

In keyhole welding, the laser process results in deep welds with narrow melt pool and HAZ width. Cooling the carbon-steel, between 800°C and 500°C, when the martensite forms are very critical for welds and for determining the microstructure changes in this thin area and hence; the HAZ boarders around the melt zone [20]. For this purpose, the present model and experimental work can be used for prediction of HAZ boundaries as a function of isothermal contours till approaching the last temperature that the microstructure changes stopped significantly. From our model, equations (6) were used to determine the point (λ) and line (μ) heat source strengths) by applying the temperature required in order to find the maximum width at that temperature to represent the HAZ lateral distance.

$$\frac{q_p U}{8\pi k K (T_m - T_0)} = \lambda$$

and

$$\mu = \frac{q\ell}{2\pi k (T_m - T_0)} \qquad (6)$$

where, q_p is the power absorbed by the point source in Watts and $q\ell$ is the power absorbed by the line source per unit length in Watts/mm.

The HAZ width is the subtraction between the maximum weld width and the maximum lateral width.

3. Experiment

A CO_2 laser beam, operating in the TEM_{01} mode, with three different powers was used to perform fifteen butt-welding joints of 12mm thick (BS4360) C/Mn steel. Table (1) shows laser and work piece parameters while Table (2) summarizes all welds measurements obtained.

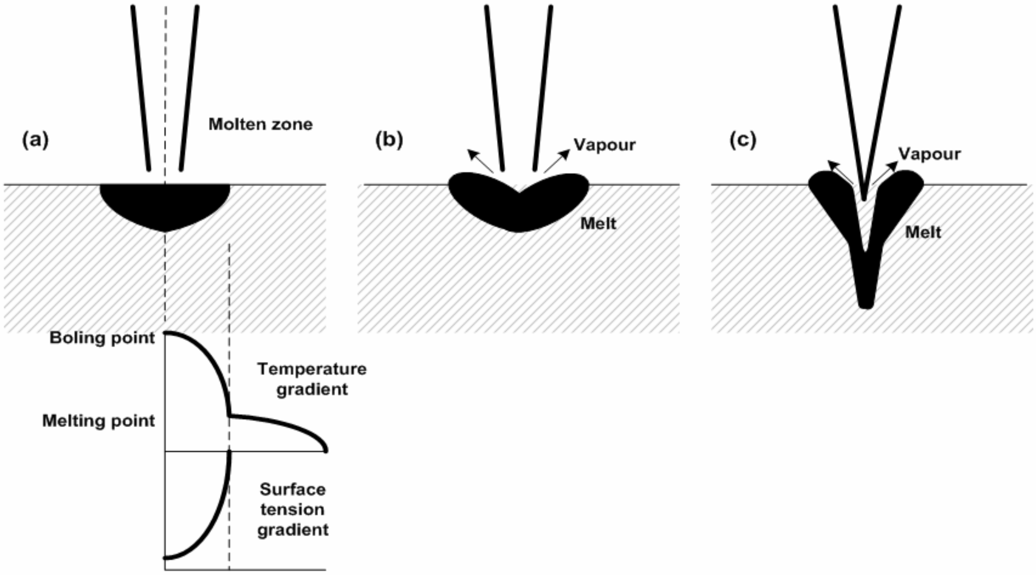

Fig. (2) The creation of a keyhole type weld pool

4. Results and Discussion

4.1. Thermal Input and Welded Area

The thermal input (P/U), defined as the laser power over the processing speed, has come out into view because of its role that conjugates both common behaviors of power and speed effects against other affected parameters such as, welded area welded depth and HAZ. Here, the cross-sectional welded area is also considered as a common factor of both maximum width and penetration depth. Thus, the importance of a plot between welded area and thermal input emerges from its collective representation of the weld profile which can be controlled by the thermal input practically.

Figure (3) illustrates this relationship where a narrow weld profile is obtained when using small thermal input while a wide profile results in from large thermal input values. It should be noticed that of up to 0.6kJ/mm, the behavior is more or less the same for the three powers (7, 8.5 and 10kW). At higher values, the welded area increases more at the lower laser power. Thermal input and welded area are more significant among other factors such as power, travel speed, top maximum width, stem width and depth to adjust the weld quality.

4.2. HAZ Results

Table (3) illustrates the HAZ values calculated at 800°C compared with the experimental values for the exact 15-samples with suitable choices of λ, μ and C. The weld maximum width of the melt pool is recorded in to recall the differences for the HAZ width measurement.

The departures that can be seen between some of the experimental and calculated HAZ values may be attributed to the ideality of the theory against different conditions that facing the experimental work. It is irrational that the HAZ is less or equal to the maximum width of the melt pool as can be seen in samples 5, 6 and 13. There are some far values from the expected listed for samples 2, 7, 8, 14 and 15. Figure (4) shows the experimental behavior of HAZ with the weld travel speed at different laser powers used, while Figure (5) shows a comparison between behaviors of the experimental and theoretical values of the HAZ lateral widths versus travel speeds for 7.0 kW input laser power. In all cases, the laser welds obtained at high travel speeds have narrower HAZ than those obtained at lower speeds.

Figure (6) shows a relationship between the HAZ and the thermal inputs at two different laser powers. As thermal input increases, the HAZ width increases too. This confirms the concept of computational adjustment between the welding parameters to produce as narrow as possible HAZ.

Table (1) Laser data and Material parameters

Laser and material parameters	Description
Laser	CO_2
Power (kW)	7.0, 8.5, 10
Mode	TEM_{01}
Focal spot (mm)	0.5
Shielding gas jet	He, flow : 50 l/min
Steel type	BS43660 C/Mn
Thickness (mm)	Steel.
Therm. conductivity k	12.0
(W/mm.°C)	0.019385
Thermal diffusivity K (mm^2/s)	12.5
Melting point (°C)	1547
Ambient Temp. (°C)	27

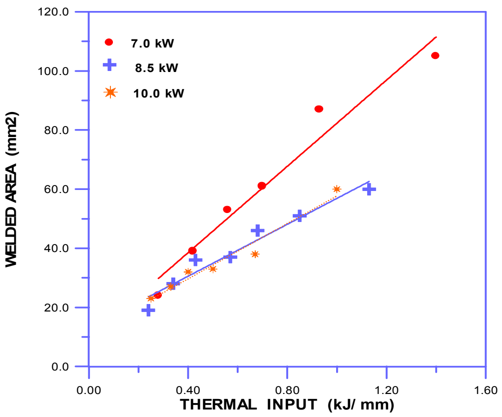

Fig. (3) Thermal input versus welded area

4.3. Temperature Fields

Figure (7) shows the isothermal contours for temperature gradient surrounding the isotherm of the fusion zones of samples (6) and (15) respectively as two different arbitrary examples. Table (4) illustrates the values of (λ) and (μ) being used to calculate each isotherm which is represented by a maximum top width and stem width for the temperatures (1547^0C, 1200^0C, 1000^0C, 800^0C, 600^0C and 500^0C) as points for temperature gradient. The c value here is considered to be zero. These fields are calculated using the present model for any temperature wanted including the three main microstructure affected temperatures that marked at both figures.

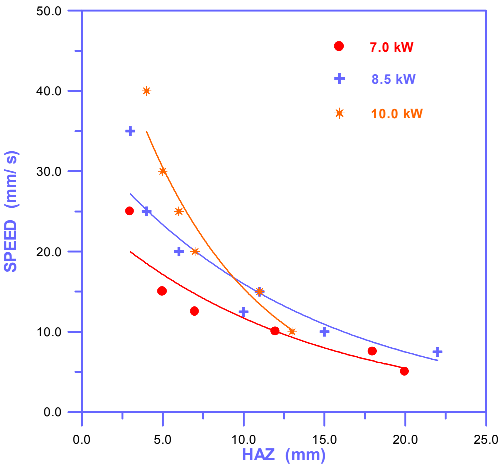

Fig. (4) Experimental HAZ versus speed at the different laser powers

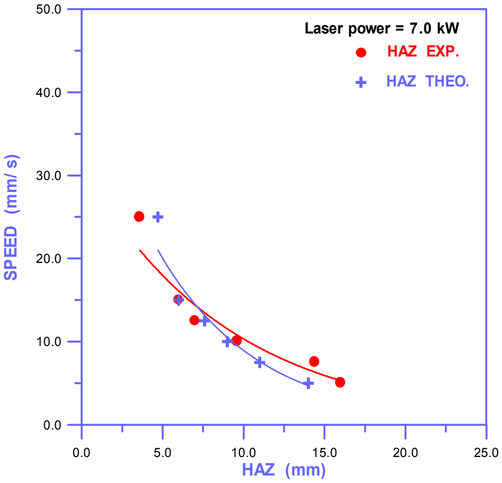

Fig. (5) Experimental and theoretical HAZ against speed at 7.0 kW laser

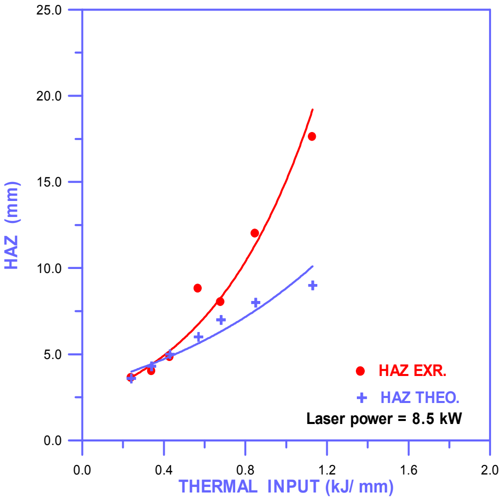

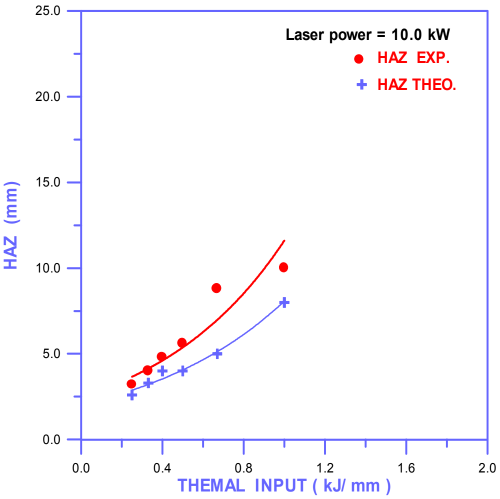

Fig. (6) Thermal input against HAZ at 8.5 kW and 10.0 kW laser powers

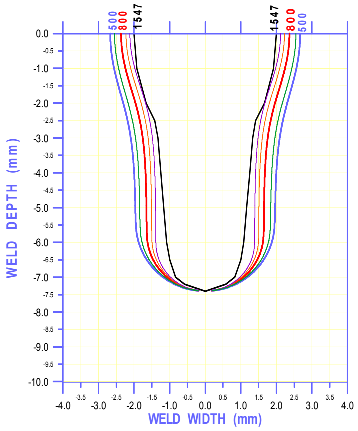

Sample (6)

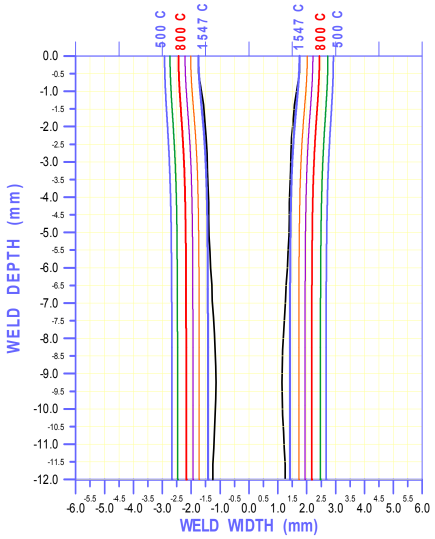

Sample (15)

Fig. (7) The isothermal contours for the calculated temperatures fields

Table (2) Laser and welds parameters used in the fifteen experiments

Experiment No	Laser Power (kW)	Travel Speed (mm/s)	Weld depth (mm)	Thermal Input kJ/mm	Max. width (mm) Expt-Cal.	Stem width (mm) Expt-Cal	Welded Area (mm^2) Exp. Cal.
1	7.0	5.0	12.0	1.40	9.5-9.54	8.0-8.04	105-105.5
2	7.0	7.5	12.0	0.93	8.0-8.06	6.5-6.52	87-87.5
3	7.0	10.0	11.0	0.70	7.0-7.08	4.0-4.03	61-61.1
4	7.0	12.5	10.0	0.56	6.0-6.02	4.5-4.5	53-52.6
5	7.0	15.0	9.3	0.47	5.0-5.08	3.3-3.3	39-39.0
6	7.0	25.0	7.4	0.28	4.0-3.96	2.5-2.47	24-23.8
7	8.5	7.5	12.0	1.13	6.0-6.0	4.0-4.1	60-60.3
8	8.5	10.0	12.0	0.85	5.5-5.56	3.0-3.04	51-51.6
9	8.5	12.5	11.8	0.68	5.05.01	2.7-2.76	46-45.8
10	8.5	15.0	11.5	0.57	4.5-4.54	2.0-2.01	37-37.7
11	8.5	20.0	11.0	0.43	4.0-4.0	2.5-2.54	36-36
12	8.5	25.0	10.0	0.34	3.5-3.57	2.0-2.01	28-27.9
13	8.5	35.0	8.5	0.24	3.0-3.05	1.5-1.504	19-19.4
14	10.0	10.0	12.0	1.00	6.0-6.04	4.0-4.02	60-60.4
15	10.0	15.0	12.0	0.67	3.5-3.5	2.8-2.84	38-38

Table (3) HAZ results calculated at 800°C compared with experimental values and maximum widths according to suitable choices of λ, μ and C

Sample No.	Laser Power (kW)	Strength of Point source λ	Strength of Line source μ	Specific location of point source C	Max. Width (mm)	HAZ Lateral Width (mm)	
						Exp.	Theo.
1	7.0	0.30	2.50	0.0	9.5	16.0	14.0
2	7.0	0.75	3.06	0.0	8.0	14.4	11.0
3	7.0	2.11	2.47	0.0	7.0	9.6	9.0
4	7.0	2.98	3.77	1.0	6.0	7.0	7.6
5	7.0	2.43	3.11	0.0	5.0	6.0	6.0
6	7.0	6.5	4.46	0.0	4.0	3.6	4.7
7	8.5	0.44	2.03	0.0	6.0	17.6	9.0
8	8.5	1.02	2.03	0.0	5.5	12.0	8.0
9	8.5	1.47	2.19	0.0	5.0	8.0	7.0
10	8.5	3.33	2.02	1.0	4.5	8.8	6.0
11	8.5	11.23	3.22	2.0	4.0	4.8	5.0
12	8.5	4.66	3.17	0.0	3.5	4.0	4.3
13	8.5	9.60	3.39	0.0	3.0	3.6	3.6
14	10.0	1.11	2.46	0.0	6.0	10.4	8.0
15	10.0	0.48	2.61	0.0	3.5	8.8	5.0

Table (4) The isotherm data for temperature values used

<table>
<tr><th rowspan="2">Sample No.</th><th colspan="4">1547°C</th><th colspan="4">1200°C</th><th colspan="4">1000°C</th></tr>
<tr><th>Λ</th><th>μ</th><th>Max. width</th><th>Stem Width</th><th>λ</th><th>μ</th><th>Max. width</th><th>Stem width</th><th>λ</th><th>μ</th><th>Max. width</th><th>Stem width</th></tr>
<tr><td rowspan="3">6</td><td>3.4</td><td>2.35</td><td>4.0</td><td>2.5</td><td>4.31</td><td>2.98</td><td>4.2</td><td>2.8</td><td>5.17</td><td>3.47</td><td>5.5</td><td>3.0</td></tr>
<tr><td colspan="4">800°C</td><td colspan="4">600°C</td><td colspan="4">500°C</td></tr>
<tr><td>6.46</td><td>4.46</td><td>4.7</td><td>3.3</td><td>8.61</td><td>5.95</td><td>5.1</td><td>3.7</td><td>10.34</td><td>7.14</td><td>5.3</td><td>3.9</td></tr>
<tr><td rowspan="4">15</td><td colspan="4">1547°C</td><td colspan="4">1200°C</td><td colspan="4">1000°C</td></tr>
<tr><td>0.251</td><td>1.371</td><td>3.5</td><td>2.8</td><td>0.32</td><td>1.74</td><td>4.0</td><td>3.5</td><td>0.38</td><td>2.10</td><td>4.4</td><td>3.9</td></tr>
<tr><td colspan="4">800°C</td><td colspan="4">600°C</td><td colspan="4">500°C</td></tr>
<tr><td>0.48</td><td>2.61</td><td>4.9</td><td>4.3</td><td>0.64</td><td>3.48</td><td>5.5</td><td>4.9</td><td>0.76</td><td>4.20</td><td>5.8</td><td>5.3</td></tr>
</table>

5. Conclusion

The focused nature of the laser spot gives rise to very narrow welds and HAZ which had been tackled in this work. With this narrow HAZ, the welded joints were completed with minimum amount of melting and heat input to the component. This has reduced thermal distortion and hence gave more accurate weld assemblies with a minimum change in the physical properties of the samples. In table (3), the HAZ obtained theoretically shows noticeable departures from practical in four samples which are: 2, 7, 8, and 15. At the same time it shows very close or relatively close results compared to practical in the rest 11 samples. If we consider the differences between ideality of the theory and the circumstances that may accompany the practical work, the results could be regarded good. Our model was used to determine the isothermal contours for temperature gradient surrounding the isotherm of the fusion zones. This gives a good picture about the HAZ lateral width during laser welding which is important when investigating the microstructure changes and accordingly the hardening and the cracks formation.

References

1. S. Chakraborty and P. Dutta, *Current Science India*, 78(7), 887-891, (2000).
2. W. Duley, **"Laser Welding"**, A Wiley-Inter Science Publication, (1998).
3. T. Forsman, "Laser welding of aluminum alloy", Ph.D. thesis, Lulea University of Technology (2000).
4. K. Nilsson, "Technical development of the Laser welding process", Ph.D. thesis, Lulea University of Technology (2001).
5. Wei Han, "Computational and experimental investigation of laser drilling and welding for microelectronic packaging", Ph.D. dissertation, Worcester Polytechnic Institute, Cambridge (2004).
6. R. Fabbro and K. Chouf, "Keyhole description for deep penetration laser welding", IIW Doc. IV-762, 212-973, (2000).
7. Sindo Kou, **"Welding Metallurgy"**, 2nd ed., John-Wiley & Sons Inc. Publications (2002).
8. J.D. Majumdar and I. Manna, *Sadhana, India*, 28(3&4) June/August (2003).
9. W.M. Steen, **"Laser Material Processing"**, 2nd ed., Springer, London (1998).
10. D.S. Hook and A. Gick, *Welding J.*, 52, 492-s to 400-s (1973).
11. K.R. Balasubramanian et al., *Adv. in Prod. Eng. Manag.*, 3(2) , 93-105 (2008).
12. M.S. Xia et al., *Sci. Technol. Welding and Joining*, 13(4), 378-387 (2008)
13. S. Venkannah and J. Mazumder "Changes in Laser Weld Bead Geometry with the Application of Ultrasonic Vibrations", Proc. of the World Congress on Engineering 2009, Vol. II, WCE2009, July 1-3, London (2009).
14. W.K. Hamoudi, A.K. Hamoudi and S.A. Salih, Iraqi J. Appl. Phys. (IJAP), 6(1), 15-23 (2010).
15. W. Duley, **"CO_2 lasers, effects and applications"**, Academic Press, London (1976).
16. J.O. Milewski and M.B. Barbe, *Weld. Res. Suppl.*, 109-s to 115s, April (1999).
17. J. Weston, "Laser welding of aluminum alloys", Ph.D. thesis, University of Cambridge, UK (2003).
18. S. Dmitriy and L.V. Zhigilei, *Phys. Rev. Lett.*, 91(10), 105701-1 to 105701-4 (2004).
19. J.D. Francis, "Welding simulation of aluminum alloy joints by finite element analysis", M.Sc. thesis, Virginia Polytechnic Institute and State University (2003).
20. P.L. Moore, "Investigation into the microstructure and properties of laser and Laser/Arc Hybrid welds in pipelines steels", Ph.D. dissertation, Darwin College, University of Cambridge, UK, (2003).

This article was reviewed at Department of Mechanical, materials and Manufacturing Engineering, Faculty of Engineering, The University of Nottingham, UK and School of Mechanical, Aerospace and Civil Engineering, The University of Manchester, UK

2nd Vacuum Symposium UK
Ricoh Arena, Coventry
18th - 19th October 2011

Sponsors

IOP Institute of Physics
Vacuum Group

IOP Institute of Physics
Ion and Plasma Surface Interactions Group

RGA user group

physicsworld

Introduction

For some time the UK vacuum community has called for an annual national meeting incorporating both technical and commercial elements. Following the successful VS-1 meeting held at Daresbury in February 2010, we wanted to build upon this foundation to provide something for everyone in our unique community: including FREE training seminars for new vacuum users, technical talks for the more experienced vacuum user and a vacuum equipment exhibition for everyone.

We are pleased to announce that the VS-2 meeting will be held at the Ricoh Arena, Coventry on 18/19 October 2011. The format of the meeting will be different to that originally scheduled to take place at Diamond / RAL in March. However, plans are well advanced and a full programme will be published by 30th June. The two days are distinct vacuum related meetings:

Tuesday 18th October 2011. RGA10 – the 10th meeting of the successful Residual Gas Analysers User Group.

Wednesday 19th October 2011. Advances in Vacuum Pump Technology.

In addition, Training Modules will be held both days as originally scheduled.

The meeting dates and venue have been chosen to coincide with ***Vacuum Expo 2011*** – a vacuum manufacturers exhibition that is held in conjunction with Photonex 2011 (Light & Imaging Technology) with 'cross over' to Thin Film technology.

The meeting is being organised by the Vacuum Symposium UK + RGA User Group committee with support from the IOP Vacuum Group and British Vacuum Council. Separate meeting rooms are being provided by Xmark Media, the exhibition organisers.

REGISTRATION to open by 30th June

Some **student travel bursaries** are available to help students to attend the meeting, these will be considered on a case by case basis. For details please email students@rgausers.org

Delegates wishing to register for this event please follow the following link Delegate Registration (Link not yet enabled)

Training in Basic Vacuum Practice is also now available FREE OF CHARGE. To register please follow the link Registration for Training (Link not yet enabled)

Companies wishing to EXHIBIT at Vacuum Expo should contact the exhibition organisers direct www.vacuum-expo.com.

FREE - Training Seminars

During the two days of the 2nd Vacuum Symposium UK we will once again be offering training seminars FREE of charge.

Our specialist trainer, **Dr. Austin Chambers**, will deliver two training seminars on each day as follows:

- **Basic Vacuum Principles**

Morning of Tuesday 18th October & Wednesday 19th October 2011

- **Vacuum In Practice**

Afternoon of Tuesday 18th October & Wednesday 19th October 2011

The training will be delivered in the form of an informal lecture/tutorial style. Places are limited and so you are encouraged to register early.

To register please follow the link Registration for Training

Accommodation

Details to be announced.

Useful Web Sites

IOP Vacuum Group
RGA User Group
ASTeC
Cockcroft Institute

Venue

The meeting will take place at the Ricoh Arena, Coventry.

How To Get There

Ricoh Arena, Coventry

Organising Committee

The Organising Committee are the trustees of Vacuum Symposium UK comprising Robin Hathaway, Joe Herbert, Sunil Patel & Steve Shannon

Meeting Organisers

Day 2: Joe Herbert - STFC
Day 1: Robin Hathaway - SS Scientific

Exhibiting Companies

Development of an Inverted Optical Tweezers with Full Motional Control

Hamsa Sridhar

Department of Electronic Engineering, Faculty of Engineering, Bangalore Institute of Technology, Bangalore, India

In this work, the purpose was to develop a working inverted optical tweezers setup, to optimize the gradient force, and to measure the drag force exerted by the setup when trapping and manipulating yeast cells three-dimensionally.

A working optical tweezers setup was created and optimized by maximizing the gradient force. Yeast cells were successfully trapped and manipulated three-dimensionally. The trap's radius of control was approximately 5µm and the stability of the trap lasted greater than an hour. Thirty percent power efficiency was achieved by careful alignment procedures. The tweezers exerted a 0.9pN force when manipulating particles on the xy-plane and a 0.4pN force when manipulating particles up the z-axis. Both forces were within the required range for optical manipulation techniques in the biological field (Wang, 1999).

Keywords: Optical tweezers, Full motion control, Gradient force, Manipulation

Received: 27 April 2010, **Revised**: 01 October 2010, **Accepted**: 01 June 2011

1 Introduction

Optical tweezers, or laser traps, were first introduced by Ashkin in the 1980s [1]. Using focused light rays, they allow the non-invasive trapping and manipulation of micro-particles in all three dimensions. Optical tweezers are used frequently in biological applications such as isolating cells and their organelles [2] or micro-manipulating cells to redirect their growth [3]. In this setup, regular yeast cells, immersed in tap water, were manipulated.

Electromagnetic radiation carries energy and momentum. An interaction between this radiation and matter can result in the transfer of linear momentum to the particle [4]. This principle is the underlying basis of laser-activated traps that confine atoms or particles in the Mie Regime, where particle diameter >> wavelength of laser beam [5].

Laser traps, more commonly referred to as optical tweezers, use a single-beam laser to transfer momentum and manipulate micron-sized particles in a fluid medium. For optimal trapping, the index of refraction of the particle must be greater than that of the surrounding medium. When a light ray passes through the particle, it refracts and the photons' velocity and momentum decrease. The change in momentum exerts a series of forces on the particle that are governed by the direction in which the light refracts – forces act in opposite reactionary pairs so when the particle causes the light to refract down, the light exerts an upward force on the particle.

According to Fig. (1), when the light rays pass through the particle, they refract and a gradient force, caused by the higher intensity rays, always pushes the particle towards the focus while the scattering force pushes the particle in the direction of propagation. Gravity always exerts a downward force on the particle [6].

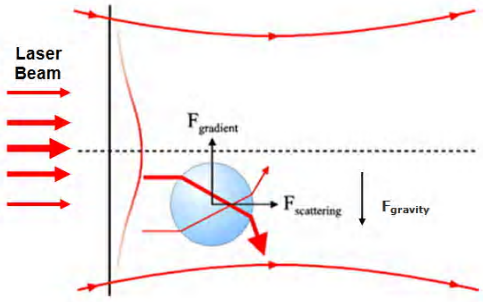

Fig. (1) The thicker arrows represent a higher intensity than the thinner ones

The key forces acting on the particle can be classified as the gradient force, the scattering force, and the force of gravity (Fig. 1). The gradient force is caused by the light's Gaussian intensity profile where the center has the highest light intensity (Fig. 2).

Force exerted when these central rays refract, causes the dominant gradient force which pulls the particle towards the focus of the beam. The gradient force acts towards the focus of the light beam (Fig. 1) and is called the restoring force as it pulls the particle towards the point of highest intensity, thereby trapping it. The stronger the net gradient force, the stronger the trap [7]. The scattering force is caused by the radiation pressure exerted in the direction that the beam travels and so this force always acts in the direction of the laser beam's propagation. The third force is the force of gravity which perpetually pushes the particle downwards.

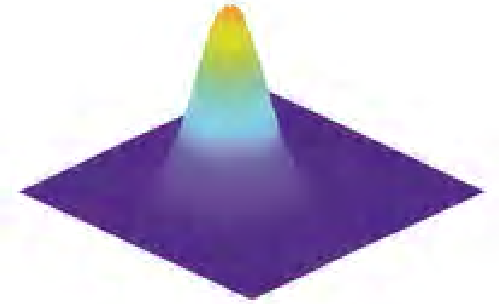

Fig. (2) The laser beam's Gaussian intensity profile makes the beam very intense in the center

As the intensity of the focus increases, the magnitude of the forces, exerted on the particle by the beam, increases. The intensity of the focus can be maximized through careful alignment procedures that ensure that the highest beam intensity enters the aperture of the objective that is used to focus the beam onto a particle.

In a regular optical tweezers, the laser is positioned above the sample and the light moves downward to trap the particle so the scattering force acts downwards, along with the force of gravity. Thus, the gradient force, which pulls the particle to a single point, thereby trapping it, must counteract both the scattering force and gravity (Fig. 3a). To create a gradient force strong enough to trap cells while counteracting these forces requires a high power laser.

Since the laser used in this project was an inexpensive one with 23mW power, an inverted optical tweezers setup was created to maximize the net gradient force produced in order to trap particles. In an inverted optical tweezers, the laser is positioned underneath the sample and the laser beam travels upward. As a result, the scattering force also acts upwards while gravity pulls the particle downwards. So, the scattering force and gravity act against each other and the gradient force compensates less for the other two undesirable forces (Fig. 3b). Consequently, the net gradient force is greater and the trap is stronger, allowing a laser of lower power to trap and manipulate particles.

The net force acting on a particle by the tweezers, or the trapping efficiency, can be gauged by measuring the maximum velocity at which a particle can be dragged by the tweezers in the fluid medium, commonly known as drag velocity. This can then be used to calculate the drag force exerted, using Stokes' equation.

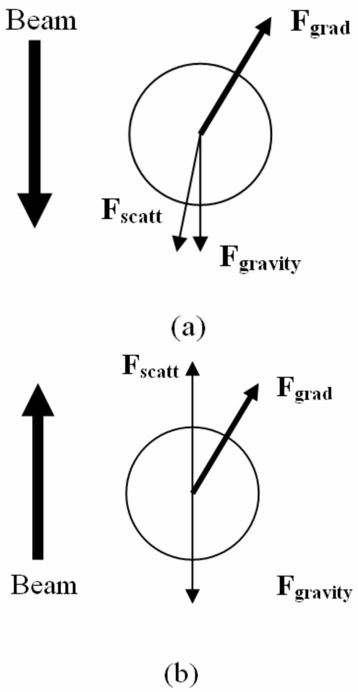

Fig. (3) (a) Regular optical tweezers: The laser beam travels down so both the scattering force and gravity act down while the gradient force has to compensate for both to push the particle towards the focus and trap it. (b) Inverted optical tweezers: The beam travels up so the scattering force acts against gravity and the gradient force compensates less for the two

Yeast cells were the chosen sample particles for trapping and manipulating. The experiment was conducted in the Mie Regime as the particle diameter, approximately 10μm for a yeast cell, is much greater than the wavelength of the He-Ne red laser beam used. Yeast cells have a greater index of refraction than water, the fluid medium in which the yeast cells were placed. Thus, incident light would refract and the gradient force necessary for trapping would be produced. Moreover, yeast cells are transparent so more light would transmit and refract, rather than reflect, increasing the gradient force exerted.

2 Design and Construction of Optical Tweezers

The laser beam emitted from the laser was collimated and was reflected off of the first gold plane mirror. It was then sent into a telescope, consisting of two lenses, where it was resized and re-collimated. The beam was then reflected off of the second mirror and was sent into the third lens (Fig.4).

The third lens converged the beam and brought it to a focus 160mm before it reflected off of a dichroic mirror (a specially coated mirror that transmits and reflects certain wavelengths of light depending on the angle of incidence) and entered the objective. The objective focused the beam onto the stage where the sample of yeast cells was placed.

The illumination light emitted from a Kohler illumination LED was focused onto the stage. Then, it passed through the objective, transmitted through the dichroic mirror, reflected off of the third mirror, and came to a focus on the CCD element 160mm away. A green filter was placed before the CCD camera to eliminate stray laser reflections entering the camera.

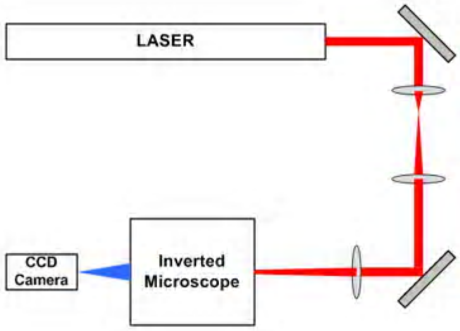

Fig. (4) The aerial view of the setup is shown. M_1, and M_2 are regular gold plane mirrors. L_1, L_2, and L_3 are plano-convex spherical lenses. The red light is the laser beam and the green light issuing from the inverted microscope into the CCD camera is the white illumination light which has been passed through a green filter

A red He-Ne laser beam with wavelength 632.8nm, 23mW power, and a partially Gaussian intensity profile, was used. Three gold plane mirrors were used to reflect the beam with attached micrometer knobs to adjust the angle of reflection in all three dimensions. Plano-convex spherical lenses were used, having focal lengths of 25.4mm, 150mm, and 170mm respectively. A dichroic mirror, which reflected 80% of He-Ne red light and transmitted regular white light incident at a 45-degree angle, was used to separate the two wavelengths of light as they both passed through the objective. The objective was 40x and had a numerical aperture of 0.85. A Nikon inverted microscope was used and a Kohler illumination LED was attached above the microscope to provide light for imaging. A CCD camera without a focusing lens was used and so the beam was brought to a focus directly on the CCD element.

The laser beam's path was carefully aligned in all three dimensions to ensure that the highest beam intensity entered the objective. Higher intensity in turn would produce a stronger gradient force on the particle, strengthening and optimizing the trap.

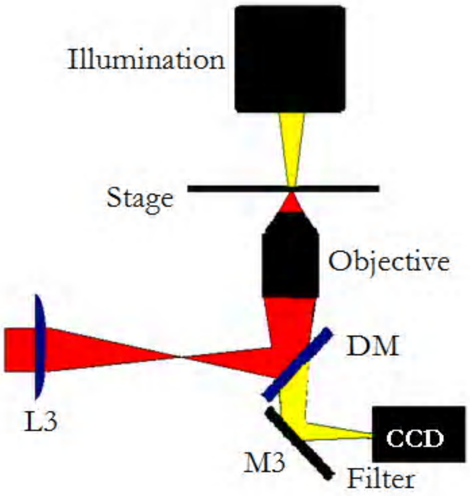

Fig. (5) The side view of the microscope is shown with the red laser beam entering from the third lens and the white illumination light (represented as yellow) emitting from the illumination above the stage and entering the CCD camera through a green filter. D_1 and D_2 are dichroic mirrors

The laser and all other optical elements were screwed into an optical table and kept at low heights to avoid vibrational aberrations and increase stability. A level was used to ensure that all optical elements, especially the laser, were perfectly horizontal.

Horizontal laser alignment was verified by measuring the vertical height of the beam just after the mirror and after a short distance away. These heights should be the same if the laser's path did not deviate from the horizontal xy-plane. Micrometer knobs were used to three-dimensionally adjust the plane of the mirror, hence the alignment of the beam, until these heights were the same.

Similarly, the lenses were placed on a translational stage with micrometers. The laser beam's diameter after exiting the first two lenses was measured both initially and after traveling a distance away. Both diameters had to be equal if the beam was collimated and this was ensured by adjusting the distance between the two lenses. Also, to verify that the lenses were exactly orthogonal to the beam, the lens reflections were checked and adjusted until they traveled straight back into the laser.

Light rays entering the objective, and later the particle, at steep angles undergo more refraction and thus exert more gradient force on the particle. To increase the gradient force, the light rays entering at steep angles should have a high intensity. However, at the same time, the total intensity of the beam entering the objective should also be maximized so that the focus has increased intensity and the trapping forces are maximized. To determine the appropriate central section of the beam that should enter the objective, the beam profile was measured.

The laser beam's profile was measured using the pin-hole method. A small hole was translated across the width of the laser beam, one thousandth of an inch at a time, and a photodetector was used to measure the intensity of the laser at each point (Fig. 6). The data was then graphed to form the beam profile (Fig. 7).

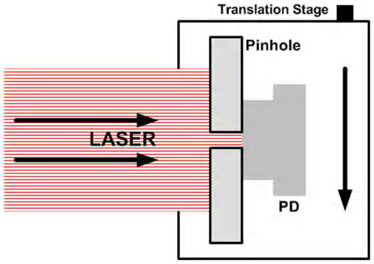

Fig. (6) The beam profile measurement was made using the above apparatus. The intensity of the laser beam across its cross-section was measured using a photo detector, one thousandth of an inch at a time

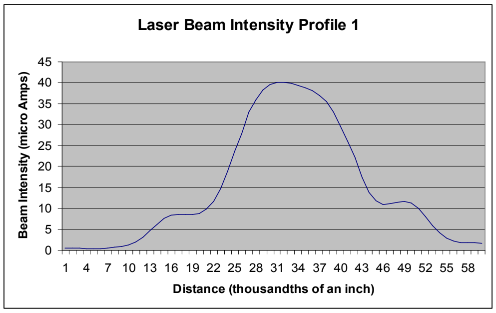

Fig. (7) The curve represents the beam's intensity profile. The part of the laser beam that isn't shaded would be the ideal part to enter the objective as the small high intensity peaks enter the objective from the steepest angles, increasing refraction and the gradient force. The central component of the beam ranges from 13 to 53: a width of approximately 40 thousandths of an inch

In contrast with a regular Gaussian curve (Fig. 2), small high intensity peaks were found at the ends of the beam profile. Since these peaks would maximize the intensity of the light rays entering the objective at the steepest angles, they were included in the desired central section of the beam to enter the objective, marked by the unshaded region (Fig. 7).

These measurements were then repeated after the laser was rotated 90 degrees, using the same pinhole method (Fig. 8). High intensity peaks are still apparent at the sides and these are incorporated in the desired central component again, ranging from 6 to 43: a width of approximately 37 thousandths of an inch.

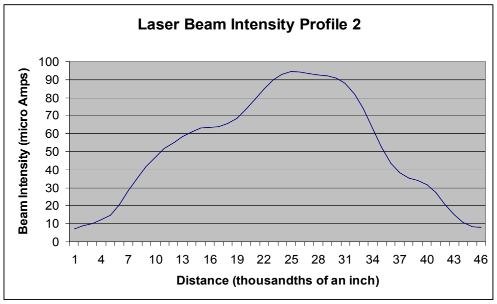

Fig. (8) The curve represents the beam's intensity profile after rotating the laser 90°

Due to the high intensity peaks found on the sides of the beam profile, the ideal central component of the beam to enter the objective was determined to have a width of approximately 40 thousandths of an inch in both measurements. This central width had to be enlarged to fill the aperture of the objective, which was 6mm wide.

The central region of the beam, determined earlier to be 40 thousandths of an inch, approximately 1.02mm, had to be expanded approximately 6 times to fill the 6mm wide aperture of the objective. This was done by creating a telescope using two plano-convex (to reduce spherical aberrations) lenses of focal length ratio 1:6. The laser beam was passed through lenses of focal lengths 25.4mm and 150mm respectively; the lenses were separated by a distance of the sum of their focal lengths – 175.4mm so that the collimated beam that entered the telescope would also leave collimated (Fig.9).

The yeast cells, immersed in water, were placed on a standard glass slide. To achieve three-dimensional trapping and manipulation, a rose chamber was created to add depth to the slide. A doughnut-shaped hole was cut in the center of a square of 100µm-thick parafilm. The parafilm square was then sealed onto a glass slide using a heat gun. The yeast cells were then placed within the chamber created by the hole in the parafilm and a Size 0 cover slip (100µm-thick) was placed on top. The glass slide was then placed upside down on the stage of the inverted microscope (Fig.10).

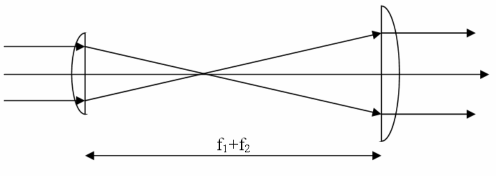

Fig. (9) The laser beam passes through the 25.4mm focal length lens and then the 150mm focal length lens. The two lenses are separated by a distance of f_1+f_2 so that the beam exits the telescope collimated again and the beam is expanded to 6 times its original width.

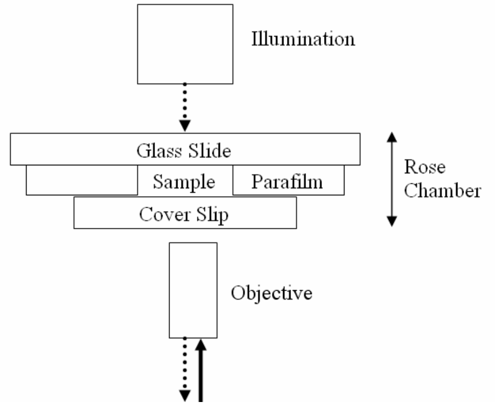

Fig. (10) The illumination light is represented by the dotted arrows. It passes through the rose chamber and exits through the objective while the laser beam, represented by the solid arrow, passes through the objective, and comes to a focus inside the rose chamber.

The yeast cells and the focus of the laser beam were imaged using a CCD camera. The white illumination light was provided by the Kohler illumination attached above the inverted microscope. The light traveled through the rose chamber and entered the CCD camera. However, the camera required an expensive long focal length lens to focus the imaging light onto the CCD element. So the original short focal length lens on the camera was removed and instead of using a focusing lens, the illumination light was brought to a focus directly onto the CCD element. As the objective was 40x, the illumination light converged to a focus 160mm after exiting the objective, which was where the camera was placed.

The laser beam and the illumination light had to follow the same path entering and exiting the objective respectively so that when the CCD camera was imaging a certain depth in the rose chamber, the focus of the laser beam would also be on the same horizontal plane. Thus, a third lens was used in the setup with a focal length of 170mm (Fig.5). It brought the laser beam to a focus 160mm before entering the objective so that it followed the same path as the illumination. The video input from the CCD camera was projected onto a standard black-and-white monitor for observation of the laser trap. The total magnification was measured to be 1750x.

3 Trapping and Calculations

In this section, the methods of trapping and manipulating the yeast cells three-dimensionally are described. Moreover, calculations measuring the power efficiency of the setup and the drag force exerted by the setup on the cells in all three dimensions are examined.

The laser beam was focused and directed into the sample. By adjusting the microscope stage until the yeast cells were in focus, the intended plane of view was obtained. From that position, the laser beam was manipulated onto a specific cell to trap it.

After trapping a particle, the focus of the laser beam was manipulated to change the direction of the gradient force, which in turn moved the particle. By slightly changing the angle of the laser beam's propagation with one of the micrometer knobs on the second mirror, the focus and the particle was moved on the xy-plane. For three-dimensional trapping, or movement along the z-axis, the distance between the laser's focus and the stage was altered slightly by turning the micrometer on the fine adjustment knob of the microscope.

The trapping distance of the trap was approximately 5µm and stability of a trapped particle lasted for more than an hour.

A power meter was used to measure the power of the laser beam after every optical element (see Fig.11). No particular optical element greatly reduced the power of the setup. Starting with 23 mW and ending with 7 mW, the setup had an overall power efficiency of approximately 30%. The 7 mW power that exited the objective exceeded the minimum 5 mW power needed to trap 10µm-diameter particles, such as yeast cells [8].

The trapping efficiency of an optical tweezers setup can be gauged by the highest velocity at which a particle can be dragged in the fluid medium by the laser's focus – the drag velocity. This can be used to calculate the net drag force that the beam exerts on the particle to manipulate it in a given dimension [9].

Stokes' equation for drag force at low velocities is:

$F_d = -6\Pi \eta r v$

where η is the fluid viscosity which is 10^{-3} for water, the medium used, r is the radius of the particle, which is approximately 5 micron for yeast cells, and v is the drag velocity.

The drag velocity of the particles was calculated by determining the maximum distance a cell could be dragged in the horizontal plane using the tweezers in a given interval of time. The distance was measured directly on the monitor and was divided by 1750 to account for the magnification. The average drag velocity was 0.01 mm/s. Thus, using Stokes' equation, the drag force exerted by the trap was 0.9 pN.

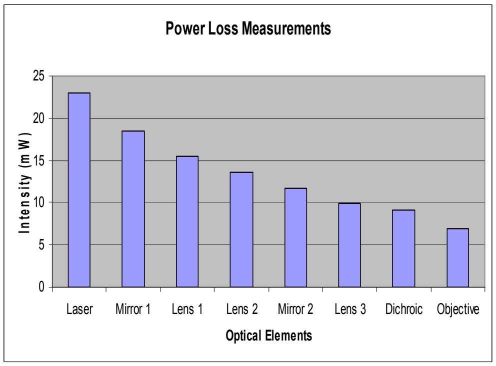

Fig. (11) The graph shows the power of the beam after each optical element. The initial power of 23 mW was eventually reduced to 7 mW as the beam exited the objective.

A similar method for calculating the drag velocity at the z-axis was used. For manipulation in the third dimension, the stage was lowered by using the micrometer on the fine adjustment knob of the microscope, thereby moving the focus of the laser beam up inside the chamber. However, due to aberrations caused by refraction, the distance the stage was lowered did not equal the distance the focus moved up inside the chamber. This difference was especially significant at high angles of incidence (Fig. 12).

Thus, an equation was created to model the distance the focus moved up, Δx, for any particular value, d, that the stage was lowered, depending on the angle of incidence of the light rays. a is the height of the cover slip (100µm) and θ is the incident angle of the light ray.

$n_1\sin\theta_1 = n_2\sin\theta_2$ *and* $n_2\sin\theta_2 = n_3\sin\theta_3 = n_1\sin\theta_1$ *by Snell's Law*

$\theta_2 = \sin^{-1}((n_1/n_2)\ \sin\theta_1)$ *and* $\theta_3 = \sin^{-1}((n_1/n_3)\ \sin\theta_1)$

$w = d*\tan\theta_1 = a*\tan\theta_2 + (x-a)*\tan\theta_3$

$x = (d*\tan\theta_1 - a*\tan(\sin^{-1}((n_1/n_2)\sin\theta_1)))$
$/ \tan(\sin^{-1}((n_1/n_3)\sin\theta_1)) + a$

Since the numerical aperture (NA) of the objective is 0.85 = nsinθ, the maximum angle at which a beam could enter the objective is 58°. The distance the focus moves up (x) for any angle of incidence (θ_1) between 0° and 58° was calculated and graphed for the stage moving distances (d) of 80, 90, and 100µm (Fig.13).

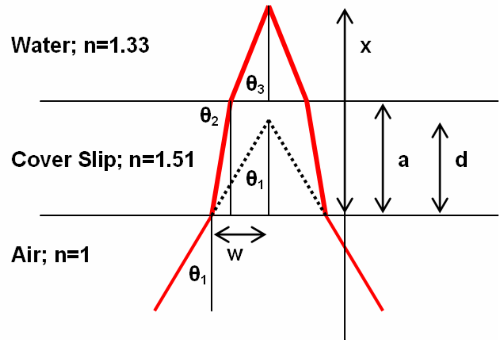

Fig. (12) The ray trace shows the path of light without refraction in dotted lines while the actual path is shown in red. The light refracts between two interfaces: air-cover and cover-water.

Fig. (13) The graph shows the distance the focus moved up (x) in microns for differing angles of incidence. The three lines show results for d = 80, 90, and 100µ.

Thus, when the stage moves up 10µm, the focus moves up 13µm (Δx) for the central rays, with low values of θ_1, and 19µm (Δx) at the steepest angles, with high values of θ_1. On average, it can be assumed the focus moves up 16µm for every 10µm the stage is moved.

Using the above calculation, the drag velocity was measured for the z-axis in the same method as that for the xy-plane and was approximately 1.14µm/sec. Using the Stokes' equation, the net drag force was 0.1pN.

However, unlike movement in the xy-plane, the gravitational force acts against upward movement in the z-axis. The velocity of a particle falling to the bottom of the chamber was measured to be 3.2µm/sec. Using Stokes equation again, gravity exerts a 0.3pN force downwards on the particle.

Thus, since the net force is 0.1pN up with gravity exerting a force of 0.3pN down, the tweezers actually exert a drag force of 0.4pN up.

4 Conclusions

A working optical tweezers setup was created and optimized by maximizing the gradient force. Yeast cells were successfully trapped and manipulated three-dimensionally. The trap's radius of control was approximately 5µm and the stability of the trap lasted greater than an hour. Thirty percent power efficiency was achieved by careful alignment procedures. The tweezers exerted a 0.9pN force when manipulating particles on the xy-plane and a 0.4pN force when manipulating particles up the z-axis. Both forces were within the required range for optical manipulation techniques in the biological field (Wang, 1999).

References

[1] Ashkin A. et al., *Opt. Lett*., 11 (1986) 288–290.

[2] Leitz G. et al., *FEMS Microbio. Lett*., 224 (2003) 97-100.

[3] Erlicher A. et al., *Proc. National Acad. Science USA*, 99 (2002) 16024-16028.

[4] Zhaohui Hu, Jia Wang and Jinwen Liang, *Opt. Laser Technol.,* 39 (2007) 475-480

[5] Wright, W.H., Sonek, G.J., and Berns, M.W, *Appl. Opt.,* 33 (1994) 1735.

[6] Wright G.D. et al., *Fungal Genetics and Biology*, 44 (2007) 1-13.

[7] Wright W.H. et al., *IEEE J. Quantum Electron.,* 26(12) (1990) 2148-2157.

[8] O'Neal, A.T. and Padgett, M.J., *Opt. Commun.,* 193 (2001) 45-50.

[9] Wang, M.D., *Current Opinion in Biotechnology,* 10 (1999) 81-86.

This article was reviewed at School of Applied Sciences, University of Technology, Baghdad, IRAQ and Department of Physics, College of Education, Islamic University of Baghdad, IRAQ

SPIE
Smart Nano+Micro
Materials and Devices

SPIE Smart Nano-Micro Materials and Devices for the Latest Micro and Nanoscale Research

Swinburne University of Technology
Melbourne, Australia
5 - 7 December 2011

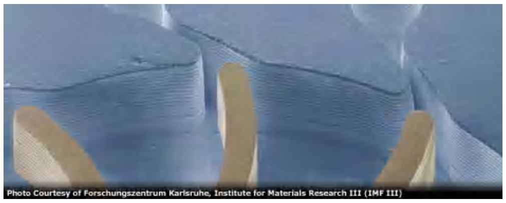

Photo Courtesy of Forschungszentrum Karlsruhe, Institute for Materials Research III (IMF III)

Call for Papers | SPIE Smart Nano-Micro Materials and Devices a multidisciplinary forum that seeks to advance research in the global use of micro- and nanofabrication technologies.
Micro and nanoscale research is enabling promising new materials and applications across many fields including air/water/food quality, energy, security, and medicine. Your work is important - submit your abstract today.

Call for Papers | Abstract due date is 30 June:

Papers will be accepted in these areas:
Devices:
- Solar cells
- Optical storage: memories, slow light
- Plasmonics
- THz applications
- MEMS/NEMS
- On-chip communications
- Lab-on-a-chip: micro-/nano-fluidics
- Bionic applications: vision aid, bionic-eye

Methods:
- Microscopies/ nanoscopies/ superresolution
- Sensing: water/food/medicine/security
- Laser processing of materials

Fundamentals (Tutorials):
- Light-matter interaction
- Plasmonics
- Lightwaves (solitons, rough waves, nonlinearities)

Materials:
- Metamaterials
- New materials for-photonics/by-photonics
- Biomimetic materials/engineering

Emerging Topics/Global Problems:
- Monitoring of global warming: ozone depletion, flood warning systems
- Water/food quality
- Early cancer detection

Special Sessions:
- Lighting revolution: all solid-state LED/OLED lighting
- Teaching of physics

Conference Chairs:
- **Saulius Juodkazis**, Centre for Micro-Photonics, Swinburne Univ. (Australia)
- **Min Gu**, Centre for Micro-Photonics, Swinburne Univ. (Australia)

Authors and Presenters
Follow these instructions to develop a successful presentation and accompanying manuscript for the conference and for publication in the Proceedings of SPIE and the SPIE Digital Library.
1. Submit an Abstract
Abstract Due Date: 30 May 2011

- Read the Conference Call for Papers and Submission Guidelines
- Then click "submit an abstract" from within the Conference
- Official notification will be sent to the contact author of accepted presentations by 29 July 2011.

Questions about your presentation? Contact Pat Wight, your SPIE Conference Programs Coordinator, or send an email to abstract_help@spie.org
2. Prepare to Present at the Conference

- Visa application information and invitation letter requests
- Prepare your presentation:
  - Oral Presentation Guidelines
  - Poster Presentation Guidelines
- Apply for an SPIE Contingency Student Travel Grant (Only full-time students may apply for a supplemental travel grant.)
- Pre-register for the conference.

Present a Better Paper: Take one of these new online courses from SPIE.
3. Prepare and Submit Your Manuscript
Publish Your Work!

- Publication of your manuscript on the SPIE Digital Library offers worldwide access within 2 to 4 weeks after the meeting
- With over 300,000 papers covering 1990 to the present, the SPIE Digital Library is the world's largest collection of research papers in optics and photonics
- Proceedings of SPIE are among the most cited references in the patent literature
- Proceedings of SPIE are indexed in numerous online databases including INSPEC, Ei Compendex, Scopus, Chemical Abstracts, SPIN, International Aerospace Abstracts, ISI Index to Scientific and Technical Proceedings, and the Smithsonian/NASA Astrophysics Data System Abstract Service (ADS)
- Articles and citations are linked via CrossRef
- Publish your manuscript with attached multimedia files in SPIE Digital Library
- After publication in Proceedings of SPIE, expand and revise your paper and submit it to one of SPIE's peer-reviewed journals (http://spie.org/journals).

Adawiya J. Haider[1]
Raad M.S. Al-Haddad[2]
Khaled Z. Yahya[1]

[1] *School of Applied Sciences, University of Technology, Baghdad, Iraq*
[2] *Department of Physics, College of Science, University of Baghdad, Baghdad, Iraq*

Nanostructure Dopants TiO_2 Films for Gas Sensing

Nanostructure TiO_2 doped with noble metals such as (Ag, Pt, Pd, Ni) thin films were prepared by Pulsed Laser Deposition (PLD) on SiO_2 and Si (111) substrates. The thin films structures were determined by X-ray Diffraction (XRD). XRD pattern shows an increase in the average size of the crystalline grains with the range (11.6-25) nm in the all film samples. The morphology properties were determined from Atomic Force Microscopy (AFM), which shows that the grain size of the nanoparticles observed at the surface depend on the type of metal dopant.TiO_2 doped with 3 % Pt metal has the smallest grain size of (11.6nm) and RMS roughness values of (28 nm). The produced thin films in this study have been exposed to 50 ppm CO gas concentration.TiO_2 doped with noble metal has sensitivity of higher than pure TiO2 .TiO_2 doped with Pt metal deposited on Si (111) has 23 % maximum sensitivity to CO gas with optimum operation temperature of 250°C.

Keywords: Pulsed-laser deposition, TiO_2 doped thin films, Nonstructural, Gas sensor
Received: 24 April 2010, **Revised**: 01 October 2010, **Accepted**: 01 June 2011

1. Introduction

Gas sensors based on semiconductor metal oxide thin films focused numerous research efforts during the last few years. Among them, titanium dioxide (TiO_2) has been investigated due to its sensing properties in front of hydrogen [1], carbon monoxide and oxygen [2], hydrocarbons [3,4], or humidity detectors [5]. Its sensing capability has been proved to improve with the addition of metal dopants as Ce and W [6], Cu [7], Nb and Cr [8], or Pt [4,9].

TiO2 exists in three crystal phases: rutile, anatase and brookite. Rutile phase TiO2 is the most common crystal phase in nature. Conversely, anatase is not as thermodynamically stable as rutile. Thus, the synthesis of pure anatase phase TiO_2 thin films is a difficult task. On the other hand, it is known that anatase possesses a higher photocatalytic activity than rutile and, thus, better gas sensing properties [10.11]. Indeed, the photocatalytic activity enhances the sensitivity of gas sensors by the photo-induced molecular transformations which take place at the catalysts' surfaces [12]. A number of recent studies have been directed to TiO_2 films doped with metal dopants like Cr, Nb, Pt, and Al [13-16]. Except for the improvement of photocatalytic properties, these dopings can also inhibit

Unwanted crystallites growth or phase transformation [17,18]. Many deposition techniques for TiO_2 films have been explored such as chemical vapor deposition (CVD) [17], atomic layer deposition (ALD) [21], and pulsed laser deposition (PLD) [19,20]. Recently, sputtering [22,18,23-25] has become the most commonly used technique for the deposition of titania due to its controllability and simplicity. Different processes may lead to different microstructure in the films prepared [26,23]. In this regard, a systematic study of the influence of sputtering parameters and post-deposition annealing will be necessary. The PLD process is particularly efficient in producing oxide thin films, while offering ease in controlling the physical, chemical and structural properties of the films [18].

In this paper, we report the successful growth of doped and undoped TiO_2 thin films on (001) SiO_2 and Si (111) substrates by PLD. Besides the structure and Morphology as a function of dopant metals, we investigated the gas sensor properties of the deposited thin films.

2. Experiment

2.1 Film preparation

The deposition was carried out using Q-switched Nd:YAG laser with a frequency second radiation at 532nm (pulse width 7ns repetition rate 10HZ) and fluencies energy 1.2 J/cm^2. The studied films were prepared by from pure TiO_2 and (1-3 wt.%) (Pt,Ag,Ni,Pd) doped TiO_2 targets films were grown by pulsed laser deposition on an optically Flat glass substrates kept an on-axis distance of 4cm from the TiO_2 target. The chamber was kept at vacuum pressure of 10^{-3} mbar as shown in Fig. (1). The TiO_2 disc was ablated from 10-100 pulses (10-20min) to get single layered thin films. During the deposition the substrate temperatures (T_s) were kept at 500°C under 10^{-1} torr oxygen pressure.

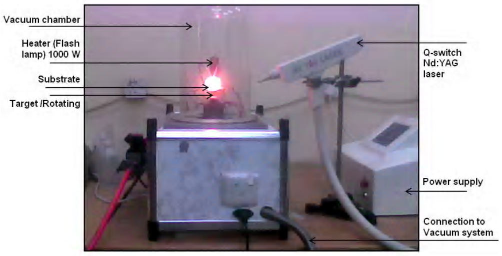

Fig. (1) Experimental setup

2.2 Film characterization

The crystalline structure of the films was determined by X-Ray Diffraction (XRD) measurements (Philips PW 1050, λ=1.54Å) using Cu kα. The surface morphology was examined Atomic force microscopy (AFM-Digital Instruments NanoScope) working in tapping mode. The gas sensor measurement by A Hewlett-Packard Systems 5890 Series II GS system. The produced thin films in this study have been exposed to 50ppm CO gas concentration.

3. Results and discussion

TiO_2 films doped with noble metals (Ag, Pt, Pd and Ni) at percent (1,2 and 3 wt %) under oxygen pressure of 10^{-1} torr, 500°C substrate temperature and 1.2 J/cm^2 laser fluence on Si (111) wafer are shown in Fig. (2). At 1wt% concentration, the film shows diffraction peaks located at $2\theta=25.28^{\circ}$ and $2\theta=37.8°$, which belong to anatase A(101) and A(004) peaks respectively, according to standard pattern of anatanse TiO_2. Rutile peak R(110) at $2\theta=27.6°$ can be observed in the XRD profile of noble metals doped TiO_2 concentration at 1wt%, as shown in Fig. (2a). The existence of rutile phase in TiO_2 could reduce the photo-catalytic activity of both the doped catalysts and increase reflectivity. Figure (2b) shows the doped TiO_2 films diffraction at 2wt% concentration of noble metals the peaks of rutile R(110) decreasing and (FWHM) increasing of anatase peak A(101). When 3wt % concentration of noble metals doped TiO_2 peaks of rutile R(110) disappear and the anatase peak A(101) increasing in (FWHM) as shown in Fig. (2). The full-width at half-maximum (FWHM) of the (110) rutile and (101) anatase peaks were also evaluated to analyze the variation of grain sizes in the films doped. From the peaks shown in Fig. (2c), it can be concluded that 3wt% (Ag, Pt, Pd and Ni) doped TiO_2 films generally have smaller grain sizes (15.7, 11.6, 21.5 and 19nm). The increased doping level of 3wt% might have to the increased potential energy of atomic diffusion barrier and further results in the inhibition of anatase to rutile transition and grain growth.

Overall, it can be seen that all XRD patterns of doped TiO_2 films did not show any significant changes. These results indicated that dopants have no effect on the anatanse structure of TiO_2 films. XRD analysis also did not detect the dopant phase. These due to the low concentration of dopants. Thus, no dopants peak can be observed in this research when the dopants concentration was (1-3wt%).

The AFM images of the TiO_2 /Si films dopant with noble metals sample are presented in Fig. (3). Thin films have been deposited at fixed substrate temperature of 500°C and at oxygen pressures of (5×10^{-1} mbar) and 1.2 J/cm^2 laser fluence energy density . The AFM images of the Ag, Pt, Pd and Ni doped TiO_2 thin films show a uniform granular surface morphology. The average grain diameter was evaluated from the plane view images at range (15-20nm). The tilted image reveals grain heights of a few tens of nanometers. The RMS roughness increases with noble metal percent due the presence of the fine dispersed phase. The samples are very rough with RMS values (28, 26, 23 and 24 nm) for thin films doping with 3% (Ag, Pt, Pd and Ni) respectively as shown in table (1).

Figure (4) shows the sensitivity as a function of operation temperature in the range (100-400°C) for TiO_2 pure and doping with noble metal at different concentrations (1%, 2% and 3%) which are deposited on glass and Si wafer (111) at fixed oxygen pressure 5×10^{-1} mbar and 1.2 J/cm^2 laser fluence energy density. It can be seen in Figure (4) that the sensitivity of all the films increases with the increasing in the operating temperature, reaching a maximum value corresponding to an optimum operating temperature which is 250°C for all the samples. Above this temperature, the sensitivity to CO gas for all sample decreases at about 400°C. The high temperature operation of the sensor make the life time of the sensor become shorter and increasing resistance thus required more electricity for operation. It is believed that the oxygen could be removed or lost from the bulk of the metal oxide materials at high temperatures. This suggests that the response of the sensor may decrease at higher temperatures since there will be more oxygen vacancies which led to less occurrence of CO oxygen reaction. The response of the undoped sensor to CO gas is relatively low, and the maximum response is (0.5 %) at 250°C.

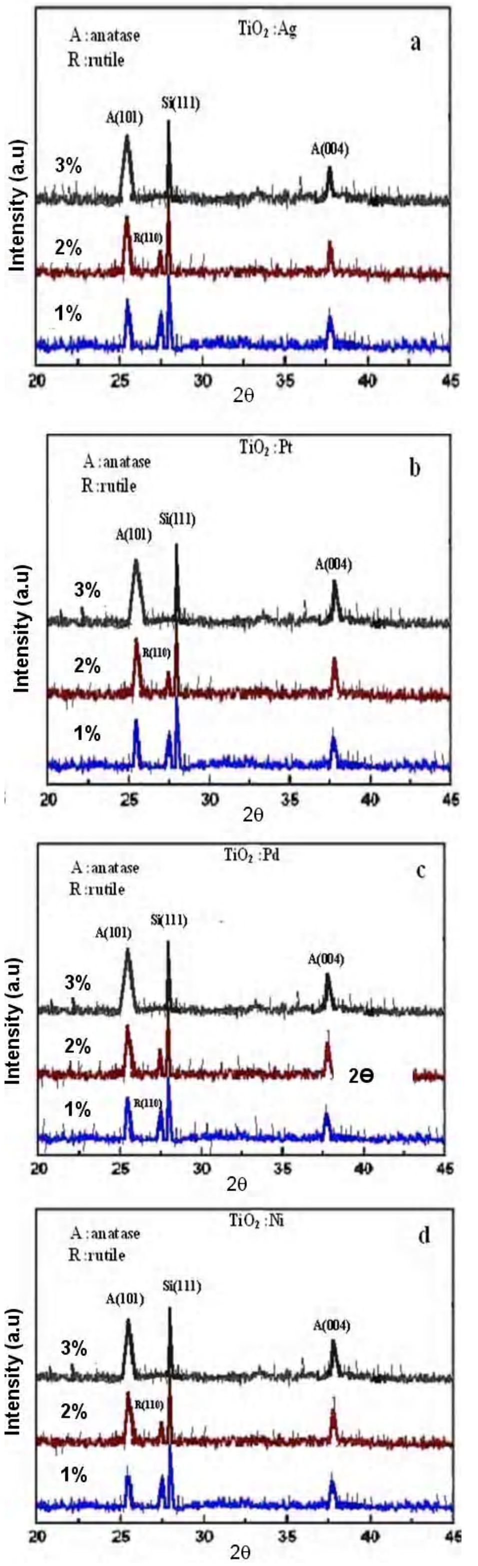

Fig. (2) XRD patterns of TiO_2 films grown on Si Doping with noble metal of (a) Ag, (b) Pt, (c) Pd% and (d) Ni

Noble metal doping(Ag, Pt, Pd and Ni) increases the sensitivity of TiO_2 sensors to CO gas and improves the sensor response at which the sensor response is maximized (3.3%) at 250°C for TiO_2 doping 3% Pt. The sensing process depends on the surface roughness which increases detection sensitivity doping TiO_2 films have higher value of sensitivity from pure TiO_2 because the surface roughness of doping TiO_2 higher than pure TiO_2.

TiO_2 deposited on silicon has sensitivity higher than TiO_2 deposited on glass as shown in Fig. (5). Table (2) shows the sensitivity values of TiO_2 pure and doping with different noble metal concentration at operation temperature T=250°C.

Table (1) Structural and morphological characteristics of the TiO_2 Pure films deposited at different noble metal doping at Oxygen pressure 5×10^{-1} mbar with 500°C substrate temperature and 1.2 J/cm^2 laser fluence

RMS roughness	AFM of plane grain size (nm)	X-ray of plane grain size (nm)	Sample
28 nm	61	15.7	TiO_2 :3% Ag
26 nm	12.4	11.6	TiO_2 :3% Pt
23 nm	23	21.5	TiO_2 :3% Pd
24 nm	20.5	19	TiO_2 :3% Ni

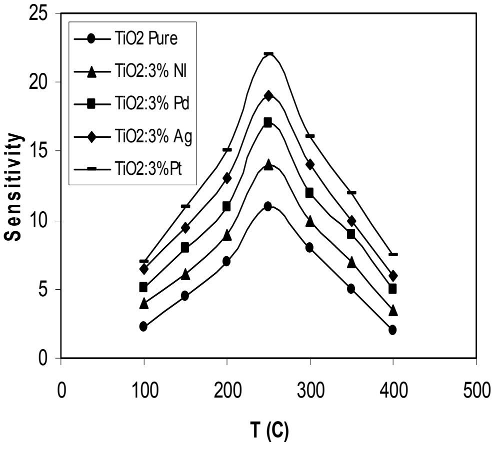

Figure (5) Sensitivity for TiO_2/Si pure and doping with 3% (Ag ,Pt ,Pd ,and Ni) films for CO gas at different operation temperature at laser fluence 1.2 J/cm^2 with O_2 pressure=10^{-1} mbar

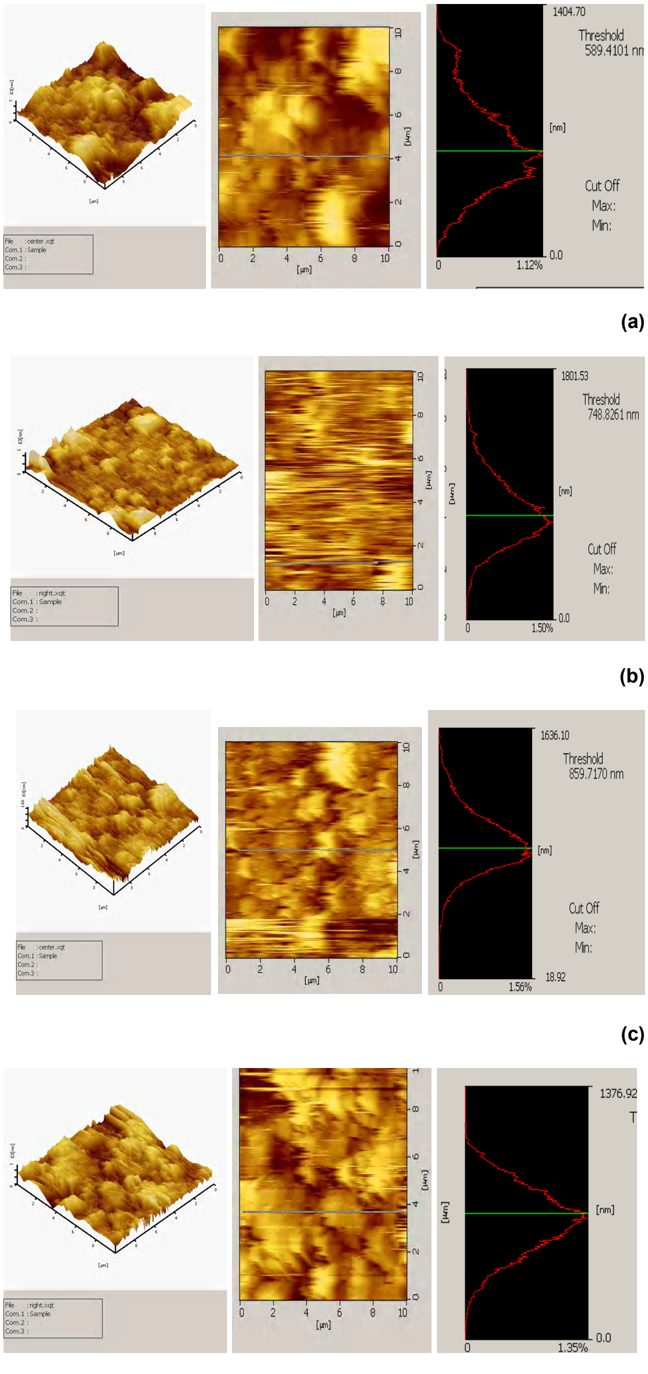

(a)

(b)

(c)

(d)

Fig. (3) AFM image of the TiO_2/Si thin films doping 3% with different noble metal (a) Ag (b) Pt (c) Pd and (d) Ni substrate temperature 500°C and laser fluence 1.2 J/cm^2 with O_2 pressure=10^{-1} mbar

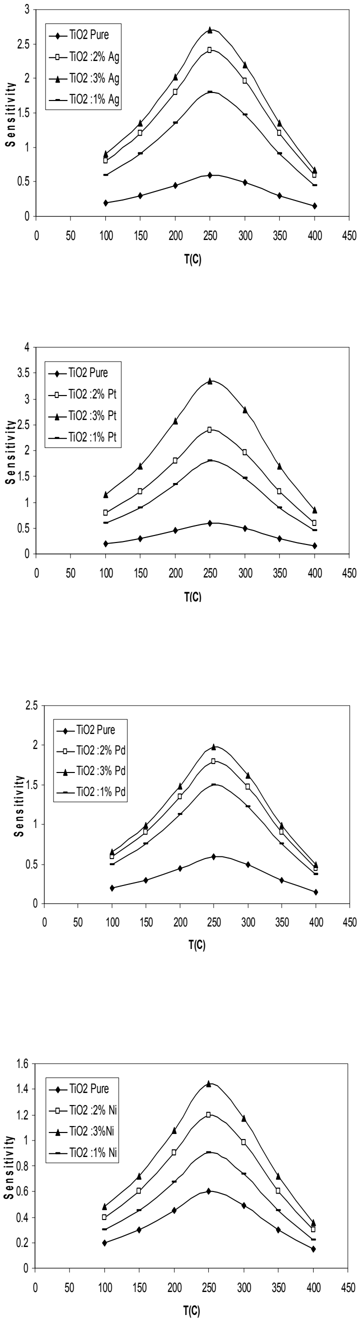

Figure (4) Sensitivity for TiO_2/glass pure and doping with 1%, 2% and 3% (Ag, Pt, Pd, and Ni) films for CO gas at different operation temperature and laser fluence 1.2 J/cm^2 with O_2 pressure=10^{-1} mbar

Table (2) Sensitivity values of TiO_2 pure and doping with different noble metal concentration at operation temperature T=250°C

Samples	Sensitivity
TiO_2 pure/glass	0.5
TiO_2 :1% Ag /glass	1.7
TiO_2 :2% Ag/glass	2.3
TiO_2 :3% Ag/glass	2.7
TiO_2 :1% Pt/glass	2.2
TiO_2 :2% Pt/glass	3
TiO_2 :3% Pt/glass	3.3
TiO_2 :1% Pd/glass	1.5
TiO_2 :2% Pd/glass	1.9
TiO_2 :3% Pd/glass	2.2
TiO_2 :1% Ni/glass	0.85
TiO_2 :2% Ni/glass	1.2
TiO_2 :3% Ni/glass	1.5
TiO_2 pure/Si	7.5
TiO_2 :3% Ag/ Si	17
TiO_2 :3% Pt/ Si	23
TiO_2 :3% Pd/ Si	15
TiO_2 :3% Ni/ Si	12.5

4. Conclusions

From the obtained results, conclusions can be made for sensing performance of TiO_2 pure and dopant it with noble metals modified sensors. Pure TiO_2 showed poor response to CO gas. TiO_2 thin film doped with 3% wt Ag, Pt, Pd and Ni was the most sensitive element to CO gas. The optimum operating temperature for CO gas sensing was 250°C. TiO_2 thin film doped with Ag, Pt, Pd and Ni would be suitable for fabricating the CO gas sensors. The sensor TiO_2 doping with Pt showed good selectivity to CO gas. TiO_2 deposit on Silicon has sensitivity to CO gas higher than TiO_2 deposit on glass

References

[1] G.K. Mor et al., *J. Mater. Res.*, 19 (2004) 628.

[2] M.L. Frank et al., *Sensors and Actuators*, B 87 (2002) 471.

[3] L. Francioso et al., *Sensors and Actuators*, B95 (2003) 66.

[4] J. Trimboli and P.K. Dutta, *Sensors and Actuators*, B102 (2009) 132.

[5] L.L.W. Chow et al., *Sensors and Actuators*, B76 (2001) 310.

[6] L. Zheng, *Sensors and Actuators*, B94 (2003) 294.

[7] N.O. Savage, S.A. Akbar and P.K. Dutta, *Sensors and Actuators*, B72 (2009) 239.

[8] K. Zakrzewska, *Vacuum,* 74 (2004) 335.

[9] I.N. Mihaliescu, *Appl. Surf. Sci.*, 252 (2006) 4568-4581.

[10] N. Ruzycki et al., *Surf. Sci. Lett.*, 529 (2009) L239.

[11] I.N. Mihaliescu, *Appl. Surf. Sci.*, 247 (2005) 429-433

[12] T.Y. Yang et al., *Rev. Adv. Mater. Sci.*, 4 (2009) 48.

[13] S.K. Hazra, S. Roy and S. Basu, *Mater. Sci. Eng.*, B 110 (2009) 195.

[14] A. Ruiz et al., *Thin Solid Films*, 436 (2008) 90.

[15] E. Gyorgy et al., *Appl. Surf. Sci.*, 252 (2006) 4578.

[16] J. Osterwalder et al., *Thin Solid Films*, 484 (2005) 289.

[17] M. Maeda and T. Watanabe, *Surf. Coat. Technol.*, 201 (2007) 9309.

[18] S.-F. Wang et al., *Appl. Surf. Sci.*, 229 (2004) 140.

[19] E. György et al., *Appl. Surf. Sci.*, 247 (2005) 429.

[20] S. Murugesan et al., *Surf. Coat. Technol.*, 201 (2007) 7713.

[21] D. Mardare, *Mater. Sci. Eng.*, 95 (2009) 83-87.

[22] D.S. Yoo et al., *Appl. Surf. Sci.*, 253 (2007) 3888.

[23] Malati, M.A. and Wong, W.K., *Surf. Technol.*, 22 (1984) 305-322.

[24] Litter, M.I. and Navio, J.A., *J. Photochem. Photobio.*, A 98 (1996) 171-181.

[25] S. Takeda et al., *Thin Solid Films*, 392 (2009) 338-344.

[26] A.I. Al-Homoudi et al., *Appl. Surf. Sci.*, 253 (2007) 8607.

This article was reviewed at Department of Electronics, University of Barcelona, SPAIN, Department of Materials Engineering, Tatung University, TAIWAN, and School of Applied Sciences, University of Technology, Baghdad, IRAQ

Workshop Technical Coordinator

Jana Kainerstorfer,
National Institutes of Health

Program Committee

Sam Achilefu, Washington Univ. School of Medicine in St. Louis
Houston Baker, National Cancer Institute
Albert-Claude Boccara, Ecole Supérieure de Physique et de Chimie Industrielles (France)
Victor Chernomordik, National Institute of Child Health and Human Development
Stavros Demos, Lawrence Livermore National Lab.
James Fujimoto, Massachusetts Institute of Technology
Enrico Gratton, Univ. of California, Irvine
Jeremy Hebden, Univ. College London (United Kingdom)
Elizabeth M. C. Hillman, Columbia Univ.
Jay Knutson, National Heart, Lung, and Blood Institute
Alan Koretsky, National Institute of Neurological Disorders and Stroke
Xingde Li, The Johns Hopkins Univ.
Dennis Matthews, Lawrence Livermore National Lab.
Nicole Morgan, NIH Division of Bioengineering and Physical Science
Josh Pfeffer, U.S. Food and Drug Administration
Brian Pogue, Dartmouth College
Kambiz Pourrezaei, Drexel Univ.
Jessica Ramella-Roman, The Catholic Univ. of America
John Schotland, Univ. of Michigan
Behrouz Shabestari, National Institutes of Health
Paul Smith, NIH Division of Bioengineering and Physical Science
Mamoru Tamura, Hokkaido Univ. (Japan)
Martin van der Mark, Philips Research (Netherlands)
Tuan Vo-Dinh, Duke Univ.
Yantian Zhang, National Institute of Biomedical Imaging and Bioengineering

Important Dates
Poster Abstracts Due:
8 August 2011

7th NIH Inter-Institute Workshop on Optical Diagnostic and Biophotonic Methods from Bench to Bedside

This 7th NIH workshop will bring together experts in the diagnosis and treatment of several important health issues we face today. The format will include lectures by top people in the biophotonics field, as well as panels of experts addressing the needs for imaging brain injury (panel 1) and the need for standardization (panel 2) of optical methods.

In addition to the invited two-day program, poster presentations are welcomed. Don't miss this opportunity to join with others to be at the forefront of efforts to discover and develop the latest light-based tools for applications to diagnose and treat disease and apply technologies to address cures in the following areas:

- Brain
- Eye
- Breast
- Image guided intervention / surgery
- Minimally invasive technologies
- Microcirculation
- Molecular Probes and Targets

This event is dedicated to and in memory of **Britton Chance**.

Workshop Chairs

Amir Gandjbakhche,
National Institutes of Health

Bruce Tromberg,
Univ. of California/Irvine

Nano/Micro Surface Texturing and Enhancing of Photovoltaic Cells Efficiency by Using UV Femtosecond Laser Pulses

Kais A. Al-Naimee

National Institute of Optical Applications,
Largo E. Fermi 6,
50125, Florence, Italy

A fast laser texturing technique has been utilized to produce micro/nano surface textures in Silicon by means of UV femtosecond laser. We have prepared good absorber surface for photovoltaic cells. The textured Silicon surface absorbs the incident light greater than the non-textured surface. The results show a photovoltaic current increase about 21.3% in toe dimension laser textured area.

Keywords: Nanostructures, Texturing, Femtosecond laser, Solar cells
Received: 11 May 2010, **Revised**: 28 November 2010, **Accepted**: 01 June 2011

1. Introduction

Lasers find widespread application in materials processing. They are successfully applied in industrial processes including welding, cutting, drilling, ablation deposition and surface treatment [1, 2]. The interaction of a high power laser beam with material has many applications including chemical analysis, micromachining and pulse laser deposition of thin films. The laser-material interaction involves complex processes of heating, melting, vaporization, ejection of atoms, ions and molecules, shock waves, plasma initiation and plasma expansion. The resulting crater and laser material interaction are dependent on the laser beam parameters (pulse duration, energy, and wavelength), the solid target properties and the surrounding environment's condition [3.]

Silicon is the most commonly used semiconductor in optoelectronic devices and silicon photodiodes are often used in industrial applications as reliable devices for light to electricity conversion. High operation Silicon photodiodes are manufactured according to their spectral responsivity. These features are especially important in the field of optical radiometry in which measurements of photometric and radiometric quantities have to be done with a high level accuracy. The description of high accuracy interpolation of quantum yield of Silicon photodiode detectors in the near UV is presented by Toomas et al [4]. The results of the of the quantum yield calculations and of measurements obtained by use of a Silicon trap detector are presented. James G. et al [5] investigated the I-V characteristics and responsivity of photodiodes fabricated with silicon that was micro structured by use of femtosecond laser pulses in a Sulfur-containing atmosphere. The Silicon surfaces irradiated with high intensity nanosecond laser pulses in the presence of Sulfur-containing gases have near unity absorption from near UV (250nm) to NIR (2500nm) at photon energies well below the bandgap of ordinary Silicon [6].

Microstructures develop spontaneously on Silicon surface under the cumulative short laser pulses irradiated in different ambient atmospheres [7,8]. The texturization of Silicon by ultrashort laser pulses enhances the absorption of light through the following phenomena [9-12]: (1) incoming light rays that are reflected from one tilted (by texturing) surface may strike another surface resulting in an increased probability of absorption, and therefore reduced reflection, (2) the light rays refracted within the silicon propagate at an angle, causing them to be absorbed closer to the junction than this process could occur in the case of planar surface which is especially relevant in material with diffusion lengths comparable to or less than the cell thickness, (3) photons which are reflected from the rear surface coming back to the front can encounter a tilted silicon surface, improving the chance of being internally reflected, either at the silicon interface or at the glass surface, and providing next chance for absorption. The third phenomenon is referred to as light-trapping, and gives an improved response especially to infrared light [13].

The silicon substrate is the most costly component in the solar cell. Reducing the wafer thickness drives down the cost as does the replacement of monocrystalline silicon with lower cost poly-silicon or mc-Si, which is made from a less energy intensive process. However, this cost efficiency comes with a price. Reducing wafer thickness risks lower strength, difficulties in handling, thermal breakage and lower light trapping capability. Mc-Si has higher metals contamination and material variability, generally poorer electrical performance, poorer structural integrity, and lower thermal stability [14]. One of the most technological methods of formation of periodically structured resistive mask is recording the interference pattern from two coherent light beams on the substrate with photoresist. Using this method, it is possible to fabricate a mask with apertures that looks like parallel strips with a period of submicrometer to a few micrometers (holographic diffraction grating). If to carry out the double exposure for two mutually perpendicular orientations of the substrate, we shall obtain a two dimensional grating, *i.e.* mask as periodically located holes or islands (depending on conditions of exposure time and etching). This technological method has been named as interferential lithography. Interferential lithography has been lately used for fabrication of one-dimensional nanostructures [15], production of the master mold for nanoimprinting lithography [16],

The paper presents results on the development of surface texturing by means of laser processing and investigation of the influence of laser texturization on the operational properties of the photovoltaic cells in order to enhance the absorption efficiency of the Silicon solar cells.

2. Experimental Part

Silicon samples had the following parameters: thickness ~330μm, resistivity 1Ω.cm and area 2x2cm. In order to decrease light reflection coefficient, front surface of the cell has been textured. The texture in the form of perpendicular grooves has been produced by means of Coherent Legend Ti: Sapphire laser facility generated horizontal linear polarised light, pulsed at a 1-kHz repetition rate, with pulse duration of 130-fs at a central wavelength of 800 nm. The output beam from the system had a laser power of ~3W in the Gaussian mode with a diameter of ~7mm. The schematic of the experimental setup is shown in Fig. (1). The laser beam was attenuated by a diffractive optic attenuator and its frequency was doubled by a BBO crystal, generating fs laser irradiation at 400nm wavelength. A smaller integrated fluence is created by neutral density (ND) filter placed between the reflection mirrors. The laser beam passed through two UV mirrors to reduce the residuals IR radiation. The laser beam was focused to ~8μm diameter by a 20X Nikon microscope objective with a 0.45 numerical aperture (NA), 10mm focal length and long working distance of 8mm. The sample under study is mounted on a PC controlled Aerotech x-y-z translation stage (ANT-25LV) of 2.5nm resolution and the fabrication process was viewed by a CCD Camera. The experiments were performed by translating the sample along the x-direction so that the laser beam scribed parallel structures, line by line along x-axis.

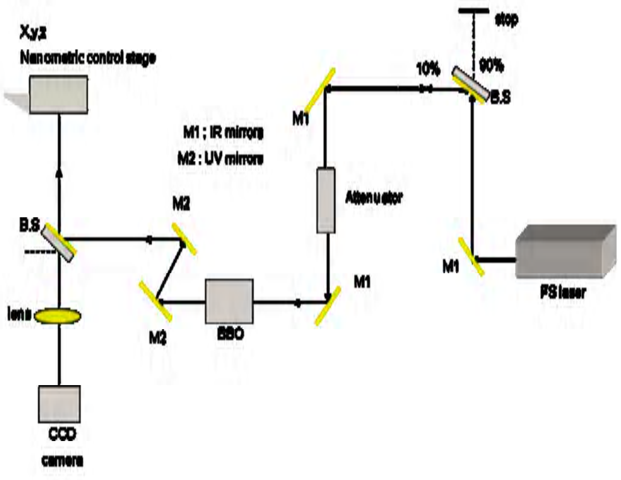

Fig. (1) Sample irradiation set-up (FS femtosecond pulse laser source, M1 IR mirrors, M2 UV mirrors)

The experiments using Si samples involved two main steps of investigation: (1) the influence of laser power variation while the irradiation spacing is constant into the sample, (2) the structural dimension created at different spacing with the fixed pulse energy while the translation speed is constant in all irradiation processes.

3. Results and Discussion

Silicon captures incident light with each pass through the bulk. As the industry manufacturers point of view, moves to thinner substrates, capture efficiency drops. To overcome this bottleneck, the structure is modified to generate a longer internal light path and to prevent the incident light from exiting the cell. A textured surface has good light capture properties to allow the light to enter the cell. The rear surface reflects internal light back into the cell substrate, Fig. (2). The texture on the front bounces internally reflected light back into the cell. In addition some cell designs will relocate the front contact to further enhance the light collection area.

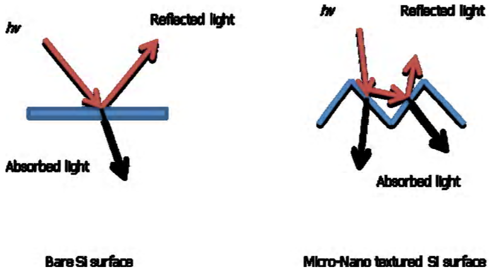

Fig. (2) Texturing effect on the light reflection and absorption

The texturing processes are commonly used to suppress optical losses, but they are optimized to absorb only at a limited wavelength range. A different method to reduce reflection is to texture the cell's surface due to the fact that texturing offers angled surfaces making some light rays bounce from one surface to another enlarging the incident photons optical path length and increasing their internal reflection. This enlarged optical path, found in textured surfaces, provides a change in the angle of incidence allowing the refracted photons to be absorbed closer to the p-n junction of the cell. This oblique coupling of light will produce an increase in the generated current.

The two-dimensional periodic structure on Si (100) surface was formed using the double exposure by two directions line mapping (irradiation), with the orientation of Si sample for two exposures differed by 90º. The value of exposures and time of selective etching were chosen so that the samples under study looked like periodically located islands of photoresist (the structure period in two mutually perpendicular directions makes 9μm). The form of hillocks was close to cylindrical. Vary spaced or close structures reduce reflectivity, so that spacing could be varied in this study is an advantageous condition. A more profound understanding of such light trapping mechanism is needed. Table (1) shows a comparison of the electrical properties of the Si cells (open circuit voltage V_{oc}, short circuit current I_{sc}, Fill Factor FF, and efficiency E_{ff}). As seen, samples even utilizing low cost technique shows 18.4 and 21.3% increasing efficiency for one dimension and two dimensions texturing. This is clear for sample with two dimensional irradiations compared with sample without irradiation.

Scanning Electron Microscope (SEM) images of the stuctures obtained in air environment. One line scan was performed at a fixed scan speed. Aperiodic structure (lines) was formed and observed in nanometer range. The SEM images shows a semi periodic structure known as ripples or grooves in submicrostructer and were found after laser irradiation, see Fig. (3). Thus, inexpensive technology using femtosecond laser pulses allows forming high-quality Si cells.

4. Conclusion

As a conclusion, we believe that the use of this approach leads to enhance Si cell efficiency. The low intensities defining the laser irradiation drastically change the scale of the surface reshaping process, promoting the formation of nanostructures and the interaction between surface roughness and/or smoothness lead to increase the number of pulses contributing certainly to rapid nanochannels formation with vary spacing. The irradiation process provides formation of Micro-Nano meter periodic structures on substrates with a large area using single or double exposition. The technology is much cheaper and simpler than the electron beam lithography.

References

[1] B. Major, "Ablation and Deposition by Pulsed Laser", Acapit, Cracow, (2002).
[2] M.J. Jackson, W.O Neill, *J. Mater. Process. Technol.*, 142, 517-525 (2003).
[3] R.E. Russo, X. Mao and S.S. Mao, *Anal. Chem.*, 74, 70A-77A (2002).
[4] T. Kubarsepp, P. Karha and E. Ikonen, *Appl. Opt.*, 39, 1 (2000).
[5] J.E. Carey et al., *Opt. Lett.*, 30, 1773 (2005).
[6] C.H. Couch et al., *Appl. Phys. Lett.*, 84, 1850 (2004).

[7] Z. Jingtao et al., *SPIE*, 10.1117_ 12.571965 (2005).
[8] R.A. Myers et al., *Appl. Opt.*, 45, 35 (2006).
[9] M. Lipiski, P. Ziba and A. Kamiski, Crystalline silicon solar cells, Foundation of materials design, Research Signpost T.C. 37-661 (2) 285-308 (2006).
[10] M. Green et al., *Solar Ener. Mater. Solar Cells*, 65, 9-16 (2001).
[11] J.F. Nijs et al., *Solar Ener. Mater. Solar Cells*, 65, 249-259 (2001).
[12] D.H. Macdonald et al., *Solar Energy*, 76 277-283 (2004).
[13] L.A. Dobrazanski et al., *J. Achiev. Mater. Manuf. Eng.*, 24(2) 179-182 (2007)
[14] Silicon Dioxide Layer Key to High Efficiency Crystalline Solar Cells, RASIRC report, 1-9 (2008). Available at http://rasirc.com/resources/whitepapers/whitepaper_solarMC.pdf
[15] S.H. Zaidi, A.S. Chu and S.R.J. Brueck, *J. Appl. Phys.*, 80(12), 6997-7008 (1996).
[16] Z. Yu et al., *J. Vac. Sci, Technol.*, B21(5), 2089-2092 (2003).
[17] V.I. Minko et al., *Semicond. Phys., Quantum Electron. Optoelectron.*, 10(1) 40-44 (2007).

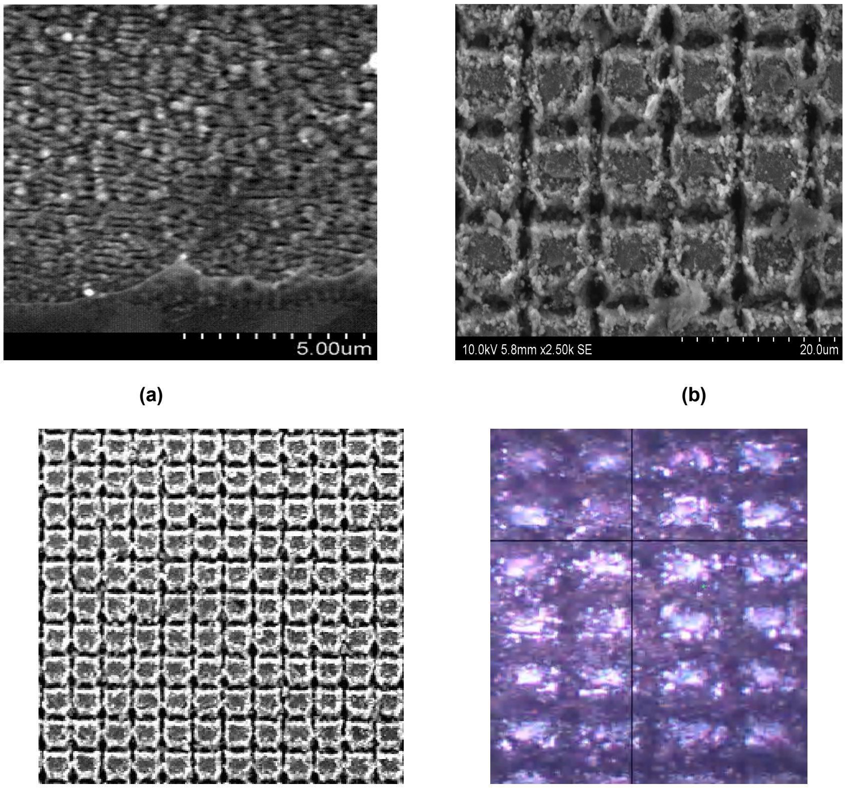

(a) **(b)**

(c) **(d)**

Fig. (3) SEM images for 1 and 2 dimensional irradiated samples (a, b, and c), and optical microscope image of 2 dimensional irradiated sample (d)

Table (1) The voltage-current parameters of the Si cell before and after irradiation process

No	Cell	I_{sc}(mA)	V_{oc}(mV0)	FF	E_{ff}
1	Without irradiation	650	580	0.68	10.3
2	1 dimensional irradiated sample	700	620	0.7096	12.2
3	2 dimensional irradiated sample	720	655	0.7404	12.5

This article was reviewed at Charles L. Brown Department of Electrical and Computer Engineering, University of Virginia, Charlottesville, VA 22904, U.S.A, and European Materials Research Society, Strasbourg Cedex 02, FRANCE

THE IRAQI JOURNAL OF
APPLIED PHYSICS
EDITORIAL BOARD

COPYRIGHT RELEASE
Iraqi Journal of Applied Physics (IJAP)

We, the undersigned, the author/authors of the article titled
…………………………………………………………………………………………………
…………………………………………………………………………………………………
…………………………………………………………………………………………………
…………………………………………………………………………………………………
…………………………………………………………………………………………………
…………………………………………………………………………………………………
that is presented to the Iraqi Journal of Applied Physics (IJAP) for publication, declare that we have neither taken part or full text from any published work by others, nor presented or published it elsewhere in any other journal. We also declare transferring copyrights and conduct of this article to the Iraqi Journal of Applied Physics (IJAP) after accepting it for publication.

The authors will keep the following rights:
1. Possession of the article such as patent rights.
2. Free of charge use of the article or part of it in any future work by the authors such as books and lecture notes without referring to the IJAP.
3. Republishing the article for any personal purposes of the authors after taking journal permission.

To be signed by all authors:

Signature:…………………………………………………..date: ………………………………

Printed name: ……………………………………………………………………………………

Signature:…………………………………………………..date: ………………………………

Printed name: ……………………………………………………………………………………

Signature:…………………………………………………..date: ………………………………

Printed name: ……………………………………………………………………………………

Correspondence address:……………………………………………………………………...
……………………………………………………………………………………………………..
Address:…………………………………………………………………………………………
…………………………………………………………………………………………………
………………………………………………………………………………………………
Telephone:………………………………...email: …………………………………………..

Note: Please complete and sign this form and mail it to the below address with your manuscript

The Iraqi Journal of Applied Physics
P. O. Box 55259, Baghdad 12001, IRAQ
Website: www.ijap.org
Email: editor@ijap.org
Phone: +964 7901274190

IRAQI JOURNAL OF APPLIED PHYSICS

CONTENTS

Instructions to Authors		2
Dipole Antenna with Fractal Koch Curve Geometry for Multiple Frequency Applications	F.J. Jibrael A.A. Sabri S.D. Sateaa	3-9
Education and Training in Optics and Photonics "ETOP2012"		10
HAZ and Melt Limits of 3-D CO_2 Laser Welding	A.K. Hamoudi W.K. Hamoudi S.A. Salih	11-17
2nd Vacuum Symposium UK		18
Development of an Inverted Optical Tweezers with Full Motional Control	H. Sridhar	19-25
SPIE Smart Nano-Micro Materials and Devices for the Latest Micro and Nanoscale Research		26
Nanostructure Dopants TiO_2 Films for Gas Sensing	A.J. Haider R.M.S. Al-Haddad K.Z. Yahya	27-31
7th NIH Inter-Institute Workshop on Optical Diagnostic and Biophotonic Methods from Bench to Bedside		32
Nano/Micro Surface Texturing and Enhancing of Photovoltaic Cells Efficiency by Using UV Femtosecond Laser Pulses	K.A. Al-Naimee	33-36
Contents		38